

RESEARCH ARTICLE

10.1029/2017JC013622

Special Section:

Sea State and Boundary Layer Physics of the Emerging Arctic Ocean

Floe Size Effect on Wave-Ice Interactions: Possible Effects, Implementation in Wave Model, and Evaluation

Guillaume Boutin¹ , Fabrice Ardhuin¹ , Dany Dumont² , Caroline Sévigny² , Fanny Girard-Ardhuin¹ , and Mickael Accensi¹¹University Brest, CNRS, IRD, Ifremer, Laboratoire d'Océanographie Physique et Spatiale (LOPS), IUEM, Brest, France,²Institut des Sciences de la Mer, Université de Québec à Rimouski, Rimouski, Quebec, Canada

Key Points:

- A spectral wave model with effects of sea ice floe size is presented
- Ice breakup is combined with three attenuations processes
- Model wave heights for a break-up event reproduce observations in Svalbard

Correspondence to:

G. Boutin,
gboutin@ifremer.fr

Citation:

Boutin, G., Ardhuin, F., Dumont, D., Sévigny, C., Girard-Ardhuin, F., & Accensi, M. (2018). Floe size effect on wave-ice interactions: Possible effects, implementation in wave model, and evaluation. *Journal of Geophysical Research: Oceans*, 123, 4779–4805. <https://doi.org/10.1029/2017JC013622>

Received 8 NOV 2017

Accepted 31 MAY 2018

Accepted article online 7 JUN 2018

Published online 10 JUL 2018

Abstract Wind waves may play an important role in the evolution of sea ice. That role is largely determined by how fast the ice layer dissipates the wave energy. The transition from a continuous layer of ice to a series of broken floes is expected to have a strong impact on the several attenuation processes. Here we explore the possible effects of basal friction, scattering, and dissipation within the ice layer. The ice is treated as a single layer that can be fractured in many floes. Dissipation associated with ice flexure is evaluated using an anelastic linear dissipation and a cubic inelastic viscous dissipation. Tests aiming to reproduce a Marginal Ice Zone are used to discuss the effects of each process separately. Attenuation is exponential for friction and scattering. Scattering produces an increase in the wave height near the ice edge and broadens the wave directional spectrum, especially for short-period waves. The nonlinear inelastic dissipation is larger for larger wave heights as long as the ice is not broken. These effects are combined in a realistic simulation of an ice break-up event observed south of Svalbard in 2010. The recorded rapid shift from a strong attenuation to little attenuation when the ice is broken is only reproduced when using a nonlinear dissipation that vanishes when the ice is broken. A preliminary pan-Arctic test of these different parameterizations suggests that inelastic dissipation alone is not enough and requires its combination with basal friction.

1. Introduction

Sea ice is rapidly changing, both in the Arctic (e.g., Stroeve et al., 2007) and in the Southern Ocean (Nghiem et al., 2016). The causes of this reduction in both extent and thickness are not fully understood and probably combine thermodynamic effects with mechanical effects. With more open water in the Arctic, wave heights have been increasing over the last 20 years (Asplin et al., 2012; Stopa et al., 2016; Thomson & Rogers, 2014). This may further amplify the evolution of sea ice.

Although research has shown that numerical wave models could be adapted to take into account wave-ice interactions (Doble & Bidlot, 2013; Dumont et al., 2011; Rogers et al., 2016; Stopa et al., 2016; Williams et al., 2013a; Zhang et al., 2016), operational forecasting models today do not allow the penetration of waves in the ice (Tolman, 2003). Indeed, a better quantitative understanding of wave evolution is needed in the transition region where wave motion is significant, usually called the Marginal Ice Zone (MIZ) (Wadhams, 1986). This MIZ can be a few hundreds of kilometers wide.

In the MIZ, waves largely determine the shape and size of ice plates, either pancakes that form during freezing or floes that are broken up by waves. In return, waves are strongly attenuated by the ice (Squire et al., 1995). The attenuation rate results from many processes that generally depend on ice thickness and floe size. Here we consider only conditions with a single layer of ice and ignore frazil or pancake ice, which are discussed by, for example, de Carolis et al. (2005), Wang and Shen (2011), and Rogers et al. (2016). Such cases are often treated with viscoelastic models in which the ice is represented either as a homogeneous viscoelastic fluid (Wang & Shen, 2011) or as a viscoelastic thin beam (Fox & Squire, 1994; Mosig et al., 2015) overlying an inviscid layer.

Instead, we focus on the interaction of waves with a layer of elastic ice that can deform and can be broken into floes, overlying a water layer with finite viscosity. As a consequence, the study presented here may not

apply to wide fields of pancakes that are found in the freezing season and but should rather be representative of waves interacting with solid ice pack. In these conditions, our goal is to explore plausible regimes of wave attenuation in the MIZ, given certain assumptions about wave-ice interaction processes.

The different mechanisms that have been proposed to explain wave attenuation in the ice can be represented by source terms in the wave action equation describing the evolution of the wave field (Masson & LeBlond, 1989). The relative importance of the different mechanisms is still unknown in conditions encountered in the natural environment (Squire, 2007). Robin (1963) measured wave attenuation in the Weddel Sea but did not conclude on its possible source, mentioning anelastic dissipation (hysteresis) and basal friction as possible explanations. Wadhams (1973) hypothesized that wave could be dissipated by secondary creep, namely, the inelastic dissipation of waves due to the ice flexure, with a strain rate proportional to the cube of the stress, following the flow law used by Glen (1955) for very slow glacier motions. The work done during and after MIZEX emphasized scattering, that is, multiple reflections of waves by floes, as the dominant source of wave attenuation (Kohout & Meylan, 2008; Kohout et al., 2014; Montiel et al., 2016). Yet, for measured long-period swells in the middle of the Arctic, Arduin et al. (2016) showed that the peaked time series of swell energy and the narrow directional spectra were not consistent with significant scattering and rather proved that the swell attenuation was dominated by dissipative processes.

Several dissipative processes can be invoked, associated with the friction of the water flowing past the ice. Basal friction occurring at the base of the ice layer is due to the relative motion of the ice and the underlying water (Liu & Mollo-Christensen, 1988). Although Liu et al. (1991) used high values of an *eddy viscosity*, analogy with boundary layers at the ocean bottom or an ice-free interface (Perignon et al., 2014) suggests that the flow should be laminar for wave heights typically under 1 m. Stopa et al. (2016) proposed a parameterization for the transition from a turbulent to laminar boundary layer in the case of random waves with Rayleigh-distributed wave heights. Unfortunately, there are no direct measurements of this oscillatory boundary layer.

Dissipation within the ice layer depends on the stress-strain relationship in sea ice. Few measurements are available at the time scales of the wave motion and with strain rates comparable to what is found in the field. Cole et al. (1998) presented laboratory experiments in which sea ice samples were cyclically loaded over a broad range of periods. With periods of 10 s, they measured a linear strain-stress relationship showing that the ice response is mostly elastic, with a measurable anelastic behavior and very little inelastic deformation. Other experiments with 10-s waves have been performed by Cole and Durrell (2001) to investigate the effects of dislocations at large strain rates. They found that dislocations are more frequent for strain rates larger than 10^{-6} s^{-1} , leading to variations of the strain rate scaling the cube of the stress, in particular for relatively warm ice at (-5°C). This inelastic behavior was later confirmed at with in situ experiments (Cole & Dempsey, 2004). For reference, a strain rate of 10^{-6} s^{-1} is the maximum value expected a 10-s period wave with a 1-cm amplitude deforming a layer of ice with a thickness of 20 cm, or a 20-s period wave with 3-cm amplitude and 2-m ice thickness. This threshold is thus routinely exceeded in wave events recorded in sea ice (e.g., Collins et al., 2015).

To our knowledge, the effect of these internal dissipation processes, anelastic (with a linear strain-stress relationship) or inelastic (with a possibly cubic relationship at strain rates above 10^{-6} s^{-1}), has not been evaluated in the context of wave evolution in the MIZ. Further, just like scattering is obviously a function of the floe size distribution, the inelastic dissipation should be strongly influenced by floe sizes as small floes are expected to tilt rather than bend. The present work thus explores the possible transition in dissipation processes as the ice is broken into floes. For this we generalize the wave-in-ice model developed by Dumont et al. (2011) and Williams et al. (2013b). In their wave model they included scattering by ice floes and ice break-up parameterization. We replace their dissipation term by a combination of the three dissipation processes identified above, namely, basal friction, anelastic dissipation, and inelastic dissipation. For consistency we update their scattering parameterization by enforcing energy conservation and we adapt the calculation of ice breakup to the use of a spectral model with possibly a broad range of wave frequencies present at the same time. The numerical treatment of all these processes is presented in section 2. Numerical simulations in simple but representative situations are presented in section 3, before moving to real cases in section 4. Discussions and conclusions follow in sections 5 and 6.

2. Physical Processes and Parameterizations

Following Tolman and Booij (1998), the wave action spectral density is discretized in wavenumbers k and directions θ as $N(k, \theta)$, with the wavenumbers corresponding to fixed frequencies f . The evolution of N on a spherical Earth with longitude λ and latitude ϕ is given by

$$\frac{\partial N}{\partial t} + \frac{1}{\cos \phi} \frac{\partial}{\partial \phi} \phi N \cos \theta + \frac{\partial}{\partial \lambda} \lambda N + \frac{\partial}{\partial k} k N + \frac{\partial}{\partial \theta} \theta N = \frac{S + S_{\text{ice}}}{\omega}, \quad (1)$$

in which the processes related to the ice are included in the energy source terms S_{ice} and ω is the intrinsic radian frequency of the waves. The various advection velocities in physical (λ, ϕ) and spectral (k, θ) spaces are given by Tolman and Booij (1998) and The WAVEWATCH III[®] Development Group (2016). The ice effects are further decomposed as scattering, anelastic attenuation, inelastic attenuation, and basal friction (Stopa et al., 2016),

$$S_{\text{ice}} = S_{\text{ice,scat}} + S_{\text{ice,ane}} + S_{\text{ice,ine}} + S_{\text{ice,fric}}. \quad (2)$$

Our basal friction $S_{\text{ice,fric}}$ combines the viscous expression by Liu and Mollo-Christensen (1988) using the kinematic viscosity of sea water at the freezing point, $\nu_w = 1.83 \times 10^{-2} \text{ cm}^2/\text{s}$, and a turbulent part defined by analogy with bottom boundary layers (Grant & Madsen, 1979), with the dissipation rate controlled by the roughness length for the wave motion. This combination is based on transition in terms of Reynolds number, with Rayleigh-distributed wave heights, each wave having a corresponding Reynolds number (see Stopa et al., 2016, for details). Note that the user can also chose to remove this transition to turbulent friction and to only keep the viscous part of the friction term. In the following study, we will refer to the full friction term (with the viscous part and the transition to turbulence) as *friction* and to the friction term only made up of the viscous part as *viscous friction*.

2.1. Wave Propagation and Energy

Following Wadhams (1973), we consider the ice as a floating continuous thin elastic plate. Solving for the linearized equations of motions, he found that the water motion is the same as under surface gravity waves without ice, with only a change of dispersion relation from the de Laplace (1776) dispersion relation without ice,

$$\omega^2 = gk \tanh(kH) \quad (3)$$

where ω is the radian frequency of the wave, k the wavenumber, and H is the water depth. This gives a phase speed $C = \omega/k$ and group speed $C_g = \partial\omega/\partial k$. Now with an ice layer of constant thickness h_i , a density ρ_i , smaller than the water density ρ_w , and an effective Young's modulus Y^* , the flexural rigidity of the ice is

$$L = \frac{Y^* h_i^3}{12(1 - \nu^2)}, \quad (4)$$

where ν is Poisson's ratio for sea ice set to 0.3. Similarly to Williams et al. (2013a), we set $Y^* = 5.5 \text{ GPa}$. With the ice cover, the dispersion relation (3) becomes

$$\omega^2 = \frac{\rho_w g k_i + L k_i^5}{\rho_w \coth(k_i H) + \rho_i h_i k_i} \quad (5)$$

where we now use the notation k_i for the wavenumber in the presence of ice. For the sake of simplicity we now assume $kH \gg 1$, giving a group speed,

$$C_{g,i} = \frac{\partial\omega}{\partial k_i} = \frac{\rho_w g + (5\rho_w + 4\rho_i h_i k_i) L k_i^4 - (3\rho_w + 2\rho_i h_i k_i) k_i^2}{2\omega(\rho_w + \rho_i h_i k_i)^2} \quad (6)$$

The stiffness of the ice thus makes the short waves relatively faster, similar to the effect of surface tension for capillary waves (Figure 1). Alternative dispersion relations are discussed by Mosig et al. (2015) and Collins et al. (2017).

Another important change in the presence of ice is the relation between the surface elevation amplitude a and the density of mechanical energy per unit horizontal surface. Indeed, due to the ice elasticity, a significant

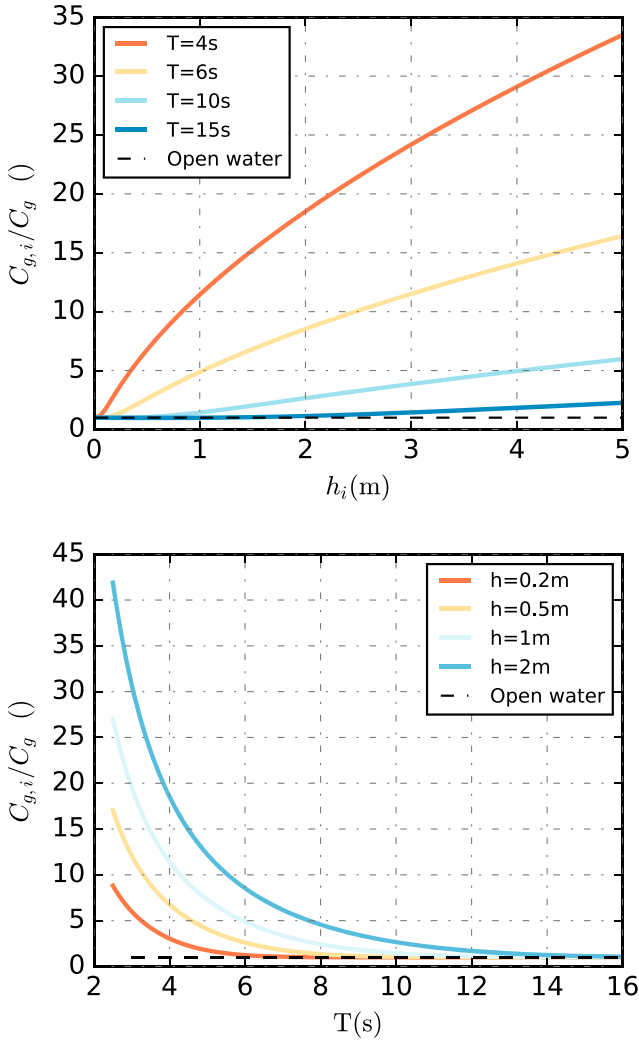


Figure 1. Top: Behavior of $C_{g,i}/C_g$ with the ice thickness in the case of deep water, that is, $k_l D \gg 1$, for four different wave periods. Bottom: Behavior of $C_{g,i}/C_g$ with the wave period for four values of the ice thickness h_i . The black dashed line represents the asymptote of the open water group velocity.

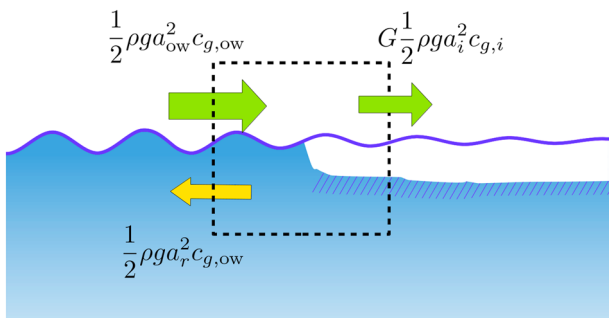


Figure 2. Wave energy fluxes for normal incidence at a straight ice edge. Defining a control volume (dashed line) around the ice edge, we can neglect dissipation when the horizontal extension of the volume goes to zero. Conservation of energy gives a relation between the wave amplitudes a , with indices r , i , and ow corresponding to reflected, ice, and open water.

part of the energy may be potential elastic energy. Wadhams (1973) defined the ratio G (called R in the original paper) of the total energy per unit surface E_t and the energy of the waves of same amplitude in the absence of ice,

$$G = 1 + \frac{4Y^* h_i^3 \pi^4}{3\rho g \lambda_i^4 (1 - \nu^2)}. \quad (7)$$

In conditions where wave energy is conserved, an amplitude a propagating from the open ocean becomes a_i in an ice-covered region, as illustrated in Figure 2. Here we will neglect refraction. Conservation of energy in a small control volume surrounding the ice edge gives the following relation between the open water incident wave amplitudes a_{ow} , the reflected amplitude $a_{r,ow}$, and the transmitted amplitude in the ice-covered region a_i ,

$$C_g \left(\frac{a_{ow}^2}{2} - \frac{a_{r,ow}^2}{2} \right) = C_{g,i} G \frac{a_i^2}{2}. \quad (8)$$

Hence, the surface elevation amplitude of short waves propagating from the open ocean to ice-covered water can be strongly reduced. This effect is important when considering the breakup of a continuous layer of ice by waves, as the wave amplitude may jump by a factor \sqrt{G} when the ice breaks. In particular, with our spectral model that extends to frequencies of the order of 1 Hz, any wind event produces short waves capable of breaking the ice if the G factor is not considered.

In order to avoid numerical errors associated to such jumps when the ice is reformed or broken, or at domain boundaries forced by inconsistent ice parameters, we have thus chosen to work, in the model, with a wave action spectrum that is multiplied by $GC_{g,i}/C_g$ and convert the spectrum on output to a measurable surface elevation spectrum, multiplying it by $C_g/GC_{g,i}$ (see Figure 3).

In the model, reflection is considered when scattering is activated. In this case, equation (8) still applies, but a represents the amplitude of the transmitted wave (Figure 2).

2.2. Wave Scattering by Ice Floes

Here we follow the general approach of Meylan and Masson (2006). After testing with a possible anisotropic scattering (see Appendix A), we use a simplified isotropic scattering source term

$$\frac{S_{ice,scat}(k, \theta)}{\omega} = \int_0^{2\pi} \beta_{is,MIZ} [s_{scat} N(k, \theta') - N(k, \theta)] d\theta'. \quad (9)$$

The simplification is that the scattering coefficient $\beta_{is,MIZ}$ is taken independent of incident and reflected directions θ and θ' , instead of directional distributions given by detailed modeling studies (e.g., Masson & LeBlond, 1989; Montiel et al., 2016). The parameter s_{scat} is normally equal to 1, but other models had used $s_{scat} = 0$ (e.g., Williams et al., 2013b) because they did not consider the directional distribution of the waves. Setting $s_{scat} = 0$ as done in other studies turns the conservative scattering mechanism into a dissipative mechanism and removes its impact on the wave directional spectrum, which is one of the key feature of this process (Wadhams et al., 1986). Also, this approximation ($s_{scat} = 0$) has a large impact on the momentum and energy fluxes that can be passed to the ocean or ice layer. The scattering coefficients $\beta_{is,MIZ}$ are estimated following Bennetts and Squire (2012). Namely, the wave reflections are treated

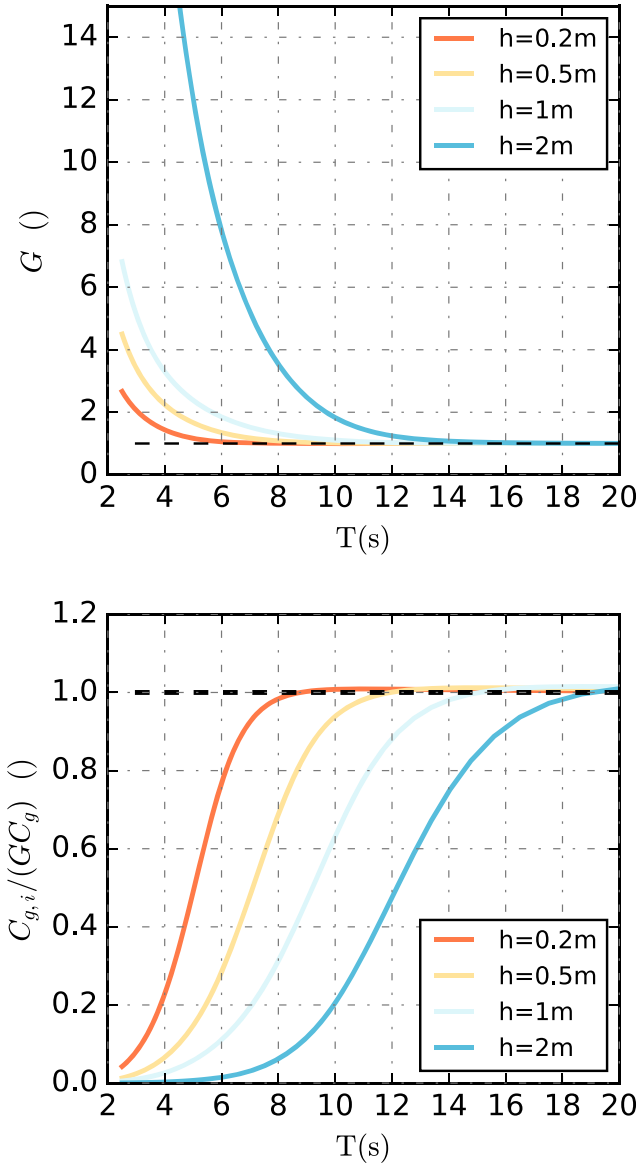


Figure 3. Top: G ratio of wave energy divided by $\rho g E$, as defined by Wadhams (1973), as a function of the wave period, in the case of deep water and for four values of the thickness h_i , 20 cm, 50 cm, 1 m, and 2 m. Bottom: Change in surface elevation variance when reflection is zero, as given by the energy flux conservation $a_i^2/a^2 = C_g/GC_{g,i}$.

model in which the value of D_{\max} would be advected and allowed to increase by freezing. The second criterion relies on Mellor (1986), which defines D_c as the minimum diameter for which flexural failure is possible. D_c is equal to

$$D_c = \frac{1}{2} \left(\frac{\pi^4 \gamma^* h_i^3}{48 \rho g (1 - \nu^2)} \right)^{1/4} \quad (11)$$

Note that we added a $1/2$ factor in Mellor's formula, as a mistake has been spotted in its hypothesis ($\sin(x\lambda) - \cos(x\lambda) = 0$ is not true for $x = \pi/(2\lambda)$ but for $x = \pi/(4\lambda)$). For the third criterion, which corresponds to the flexural strain threshold, the critical strain for the flexural failure of a thin elastic plate is

$$\epsilon_c = \frac{\sigma_c (1 - \nu^2)}{\gamma^*} F_{\text{break}} \quad (12)$$

as a succession of reflections at straight interfaces between open water and ice or between ice plates of different thickness, with waves propagating perpendicular to the ice edge. Bennetts and Squire (2012) improved the method of Kohout and Meylan (2008), which does not require the use of Monte-Carlo simulations. The $\beta_{\text{is,MIZ}}$ coefficients are computed statistically for a given range of ice thickness values allowed for the ice plates. In our model, this range is [0.25 m, 8.25 m] and aims to represent the variety of ice thickness that can be encountered in the MIZ. The number of reflections is a function of the ice concentration, and the mean floe diameter $\langle D \rangle$. This value $\langle D \rangle$ is determined by assuming a power law distribution of the floe diameters, a minimum value D_{\min} and a maximum value D_{\max} that is related to the breakup of ice by the waves,

$$\langle D \rangle = \frac{\gamma}{\gamma - 1} \left(\frac{D_{\max}^{-\gamma+1} - D_{\min}^{-\gamma+1}}{D_{\max}^{-\gamma} - D_{\min}^{-\gamma}} \right) \quad (10)$$

Here we use $\gamma = 2 + \log(\xi)/\log(2)$ with $\xi = 0.9$, where ξ is the fragility as defined in Dumont et al. (2011).

Previous waves-in-ice model (e.g., Dumont et al., 2011; Williams et al., 2013b) fixed $D_{\min} = 20$ m. It is the lower limit set in Kohout (2008). These limits correspond a transition for small floes that tilt and not bend when the sea surface is deformed.

Kohout (2008) estimates that transition occurs for wavelengths which are more than 2 or 3 times longer than the floe length. $D_{\min} = 20$ m corresponds to the critical size she estimated for waves with period $T_p = 6$ s. As our model generally includes waves with periods less than 6 s, we adapted this criterion by defining $D_{\min} = C_\lambda \lambda_i$ with $C_\lambda \approx 0.3$. The impact of having a varying D_{\min} compared to a constant one is, however, quite limited (not shown here) and does not affect the conclusions of this study.

2.3. Ice Breakup

The value of D_{\max} is determined from the local sea state, after searching for the shortest waves with wavelength λ_i that are able to break up the ice, giving $D_{\max} = \lambda_i/2$ if and only if the three following criteria are met:

1. $\lambda_i/2 \geq D_{\min}$.
2. $\lambda_i/2 > D_c$, where D_c is the critical diameter, which depends on ice properties, below which it is assumed that no flexural failure is possible.
3. $\epsilon(\lambda_i) > \epsilon_c$, the maximum strain due to the incoming wave has to be greater than a defined critical strain.

For the first criterion, ideally we would also impose that D_{\max} can only be reduced over time, but this is only possible when using a coupled wave-ice

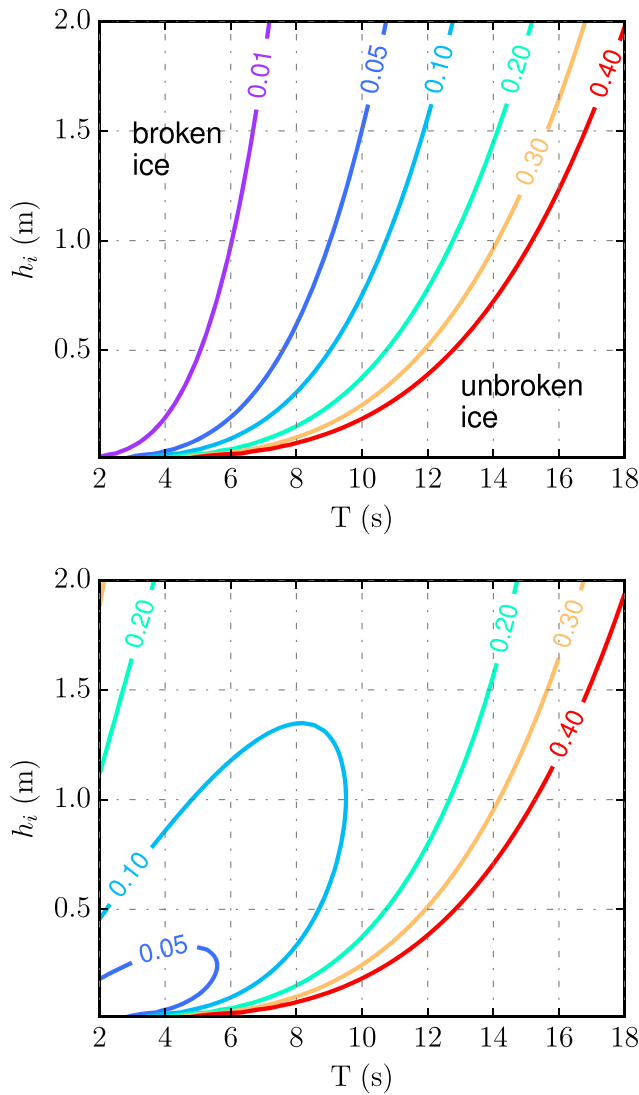


Figure 4. Minimum significant wave height (H_s) triggering flexural failure without accounting for the energy flux conservation (top) and with the energy flux conservation (bottom) as a function of wave period T (s) and ice thickness h_i (m), in the case of a narrow wave spectrum.

where σ_c is the ice flexural strength ($\sigma_c = 0.27$ MPa; Williams et al., 2013b). F_{break} is the ratio of the maximum value of the strain to its root-mean-square value. In general, this ratio is a weakly increasing function of the duration considered. Here we estimated $F_{\text{break}} = 3.6$ by considering the expected maximum amplitude in the succession of $N \approx 500$ waves with Rayleigh-distributed amplitudes, during the time over which the sea state is approximately constant.

The horizontal strain caused by waves is

$$\epsilon = \frac{h_i}{2} \frac{\partial^2 a_i}{\partial x^2}. \quad (13)$$

Accounting for the elastic energy introduces a very important correction in the local amplitude a_i of the sea surface elevation which is reduced by a factor $1/\sqrt{G}$ which is large for thick ice and short waves. It is an important difference with Williams et al. (2013b), in which the difference in wave amplitude within and outside the ice cover is accounted with the factor $W = k|T|/k_i$ where $|T|$ is the transmission coefficient for a semi-infinite ice sheet. The other difference is the use of a scale-dependent strain defined with a partial integration of the spectrum over neighboring wavenumbers, similar to what is used for wave breaking (Banner et al., 2000; Filipot & Ardhuin, 2012). The benefit of this definition is that it allows to test separately the impact of the different scales of the wave field (e.g., swell and wind seas) and to define the floe size according to the wavelength of those waves for which the surface curvature is large enough. Since our wave spectrum is formulated in energy and not surface elevation variance, the surface elevation variance is reduced by a factor $C_g/GC_{g,i}$ and this gives

$$\epsilon^2(\lambda_i) = \left(\frac{h_i}{2}\right)^2 \frac{C_g}{GC_{g,i}} \int_{0.7k_i}^{1.3k_i} k_i^4 \omega N(k) dk \quad (14)$$

where h_i is the ice thickness and $k_i = 2\pi/\lambda_i$ and $F(k)$ denotes the spectrum of the variance of the wave elevation integrated over all the directions θ .

The update of D_{max} is a two-step process. First, the shortest wavelength $\lambda_{i,\text{min}}$ for which the condition $\epsilon(\lambda_i) > \epsilon_c$ is fulfilled is computed. Then, to account for the possibility of having a narrow spectrum, the selected wavelength ($\lambda_{i,\text{break}}$) is the one for which the associated wavenumber $k_{i,\text{break}}$ follows

$$\omega_{\text{break}} N(k_{i,\text{break}}) k_{i,\text{break}}^4 > \omega_p N(k_{i,p}) k_{i,p}^4, \quad \forall p \in \mathbb{N} | 0.7k_{i,\text{min}} < k_{i,p} < 1.3k_{i,\text{min}} \quad (15)$$

In summary, our implementation of wave-induced sea ice breakup extends the work of Williams et al. (2013b) by

1. accounting for the effect of elastic energy on the reduction of wave elevation amplitude in unbroken ice with the factor we call G , derived from Wadhams (1973). As shown in Figure 4, it considerably affects the maximum wave heights for ice breaking.
2. taking into account the random distribution of wave heights as we use the expected maximum local strain, instead of the frequently exceeded root-mean-square value.

In practice, these changes are very important. Although the second modification can be absorbed into empirical calibration factors, the first correction considerably reduces the unphysical breakup that would otherwise happen due to even very low level of energy in the high-frequency part of the spectrum (Figure 4). Indeed, the version 5.16 of WAVEWATCH III uses a wind input that is scaled by the ice concentration, so that even with 98% ice concentration in the middle of the Arctic, there is still a little energy that could lead to a spurious breakup

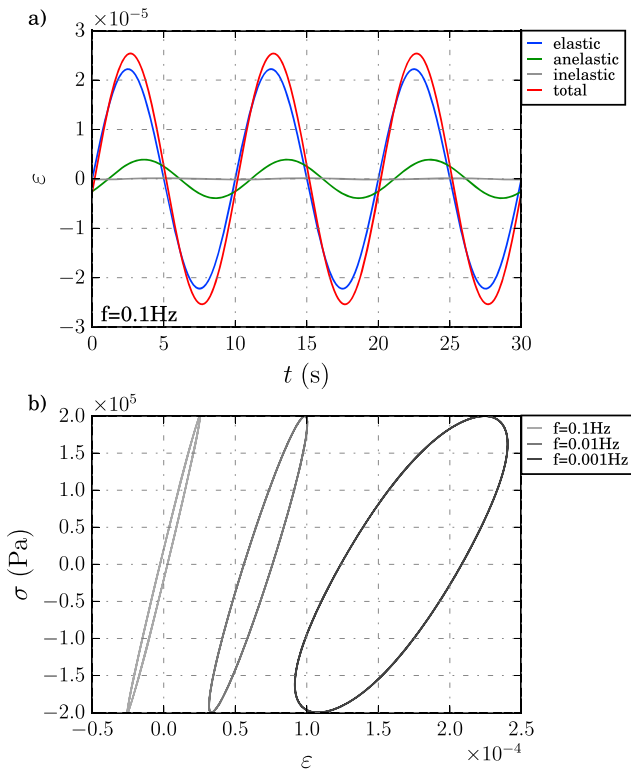


Figure 5. (a) Elastic, anelastic, inelastic, and total strain achieved with Cole (1995) model as a function of time for the cyclic loading of sea ice at a frequency $f = 0.1$ Hz with a peak stress $\sigma = 0.2$ MPa. (b) Strain stress diagram for the same cyclic loading of sea ice at three different frequencies. The area of the $f = 0.1$ -Hz ellipse is visibly not 100 times smaller than the area of the $f = 0.001$ -Hz ellipse.

of the ice. Physically, taking into account the energy flux conservation makes short waves unable to deform thick ice, as most of their energy goes into the elastic deformation of the ice. This is not the only approach to generate a floe size distribution and relies strongly on the hypothesis that the floe size obeys a power law. In fact the most important parameter is D_{\max} , and the distribution is only used for the scattering term. Horvat and Tziperman (2015) suggest an explicit way to compute the floe sizes resulting from a wave event but computationally more demanding.

2.4. Anelastic Attenuation

Cole et al. (1998) illustrates the behavior of sea ice when submitted to a cyclic loading. For the frequency range of interest, from 0.003 to 0.3 Hz, the elastic deformation dominates, but the hysteresis loop visible on strain-stress diagrams also indicates an anelastic behavior. Cole (1995) has shown that this anelastic straining results mainly from an oscillatory motion of dislocations, with grain boundaries being important at higher frequencies, and proposed a model of the anelastic behavior of sea ice. This model allows us to compute the loop area of the strain-stress diagram (Figure 5), which is proportional to the energy dissipated into heat during one cycle. Following the steps detailed in Appendix C we get

$$\beta_{\text{ane}} = \frac{A}{6} \left(k_i^2 \frac{Y^*}{(1-\nu^2)\rho g G} \right)^2 h_i^3 \frac{C_g}{G C_{g,i}} F_\lambda \quad (16)$$

with F_λ an empirical factor that varies with D_{\max} and λ_i and reduces the strain if the ice is broken into floes shorter than the wavelength. In this situation, floes tilt instead of bending, giving a negligible anelastic attenuation. We expect a relatively smooth transition of the dissipation, when averaged over many floes, from a zero dissipation for $\lambda_i \gg D_{\max}$ to the full dissipation rate given by $F_\lambda = 1$. We have thus chosen a form

$$F_\lambda = \tanh \left(\frac{D_{\max} - C_\lambda \lambda_i}{0.2 D_{\max}} \right), \quad (17)$$

where $C_\lambda \simeq 0.3$ (same tuning as for D_{\min} in 2.3) is an adjustable parameter, and the width of the transition was arbitrarily set to $0.2 D_{\max}$.

The A coefficient in equation (16) is given in equation (C1). It is a function of the ice temperature T_{ice} and on the activation energy Q_v of the dislocation process. The anelastic source term for the ocean waves is thus

$$\frac{S_{\text{ice,ane}}}{\omega} = -\beta_{\text{ane}} N. \quad (18)$$

Figure 6a shows how β_{ane} varies with the activation energy Q_v . An increase of 0.05 eV reduces the attenuation by 1 order of magnitude. This is a major source of uncertainty, and values reported in Cole (1995) are as high as 3 eV for $T_{\text{ice}} > -10^\circ\text{C}$. Cole and Durell (2001), however, applied the model for temperatures up to -5°C . As we expect sea ice temperature in the MIZ to be close to this latter value, we chose -5°C as the default value associated with the activation energy suggested in Cole (1995; 0.55 eV).

Figure 6b illustrates the effect of temperature. For temperatures between -10 and -2°C in the MIZ, the attenuation increases with the temperature, of the order of $10^{-4} \sim 10^{-3} \text{ m}^{-1}$ for waves between 0.1 and 0.2 Hz. Note that this is considerably higher than the typical values of attenuation coefficients for scattering or friction that are generally of the order of $10^{-5} \sim 10^{-4} \text{ m}^{-1}$. Ice temperature can also modify the dislocation density, which was assumed constant in Cole (1995) and may lead to a stronger variability. Finally, Figure 6c shows the thickness dependency of $\beta_{\text{anelastic}}$ (note that in equation (16) k_i , G , and $C_{g,i}$ are all functions of h_i). The maximum values of the attenuation coefficient are not affected much by changes in the ice thickness, but they show a remarkable shift toward low frequencies when the thickness increases. Besides this shift, the frequency range for which the attenuation is maximum tends to widened when the thickness decreases. As a consequence, thick ice ($h_i > 50$ cm) damps wave frequencies in the range [0.05 Hz, 0.15 Hz], while thin ice ($h_i < 50$ cm) mostly dissipates waves within [0.2 Hz, 0.4 Hz] in about 100 m.

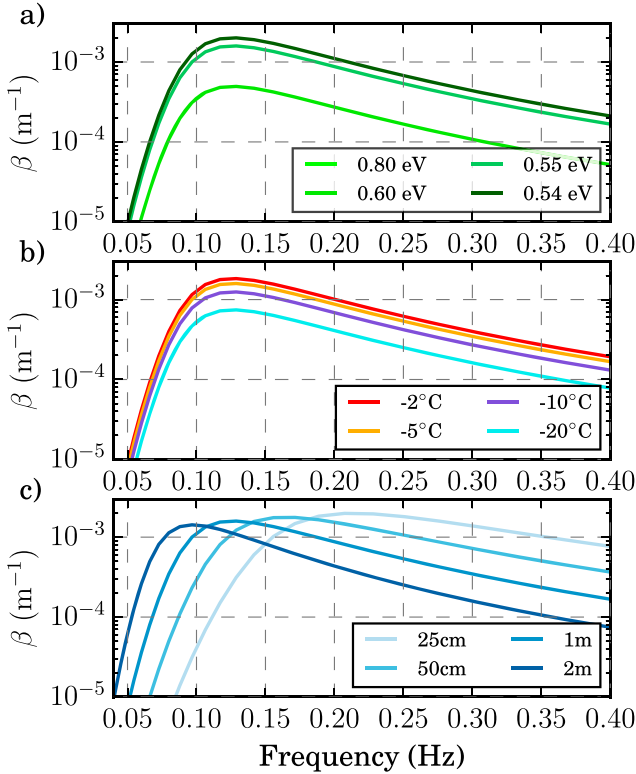


Figure 6. Sensitivity of the anelastic attenuation coefficient to the activation energy (a), the ice temperature (b), and the ice thickness (c). The default values of the activation energy and the temperature in this study are respectively $Q_v = 0.55$ eV and $T_{ice} = -5^\circ\text{C}$. The ice thickness h_i is set to 1 m in plots (a) and (b).

Cole et al. (1998) strain-stress diagrams do not show any mark of viscous deformation during cyclic loading of frequency above 0.01 Hz, and the Cole (1995) model predicts a very negligible contribution of the inelastic strain to the total strain for the same frequencies (Figure 5). Cole and Durell (1995), however, note that for high temperatures ($> -5^\circ\text{C}$) and stresses close to the flexural strength, the anelastic strain tends to be not linear anymore with the applied stress but tends toward a cubic dependency. It is supposed to be due to the fact that above a certain threshold, the dislocation density increases quadratically with the applied stress. This is confirmed in Cole and Dempsey (2004), in which the authors applied a cyclic loading compression to an in situ ice floe and observed a viscous (inelastic) deformation of the ice, for which strain-stress dependency follows a n power law with $1 \leq n \leq 3$. An inelastic attenuation law was therefore included in this study.

2.5. Inelastic Attenuation or Viscous Creep

Wadhams (1973) was the first to propose a nonlinear strain-stress relationship that could explain the observed attenuation of waves in the pack ice. He heuristically used the flow law proposed by Nye (1953) for glaciers

$$\left(\frac{d\epsilon}{dt}\right)_{ij} = \frac{\tau^2}{B^3} \sigma'_{ij} \quad (19)$$

where τ is the shear stress, σ'_{ij} is the components of the deviatoric stress tensor, and B is the flow law constant, which is a function of ice temperature. We will use $B = 10^7 \text{ N m}^{-2} \text{ s}^{1/3}$, which is in the order of magnitude found by Wadhams (1973). With details given in Appendix B, this gives a temporal decay coefficient for the wave energy that is

$$\beta_{ine} = \frac{3}{160} B h_i^5 \left(\frac{\gamma^*}{2B(1-\nu^2)} \right)^4 k_i^4 \frac{C_g^2}{\rho g C_{g,i} G^2} F_\lambda \int_{0.7k_i}^{1.3k_i} k_i^4 F(k) dk \quad (20)$$

where F_λ is transition factor given in equation (17). Finally, the inelastic source term can be expressed as

$$\frac{S_{ice,ine}}{\omega} = -\beta_{ine} N. \quad (21)$$

A justification for such a nonlinear stress-strain relationship can be found in the measurements of Cole and Durell (1995) and Cole and Dempsey (2004), with the activation of many dislocations at strain rates larger than 10^{-6} s^{-1} . We have thus chosen to evaluate the consequences of this possible inelastic effect.

2.6. Numerical Implementation

Our implementation of wave dissipation and scattering effects in the WAVEWATCH III model (The WAVEWATCH III® Development Group, 2016) corresponds to the addition of dissipation and scattering term in the wave action equation. Another important change introduced in the model is a splitting of the ice source terms from the more usual source terms of wind-wave generation, four-wave nonlinear evolution, and wave breaking. With this splitting, the ice source terms are integrated with an implicit method that is well suited for quasi-linear terms, including scattering (see Appendix A). Wave generation and wave breaking are allowed in partially ice-covered seas. Their associated source terms are scaled by $(1 - c_i)$, with c_i the ice concentration, to account for the fact that the ice cover prevents the momentum to be transferred from the atmosphere to the ocean. Ice source terms are all scaled by c , with the exception of scattering, as they only apply in the presence of ice. Scattering source term already contains the ice concentration dependency into its formula.

3. Effects of Different Processes Taken Separately

To investigate the effects of the attenuation and ice break-up processes, separately and combined, idealized simulations were realized on a grid with 100×40 nodes, with a 12.5-km resolution. Each test starts with waves radiating into the domain at $x = 0$. Wave radiation is centered at the middle of the y axis. The model domain is free of ice over the first 10 km, after which the ice concentration increases linearly from 0.4 to 1, as x increases

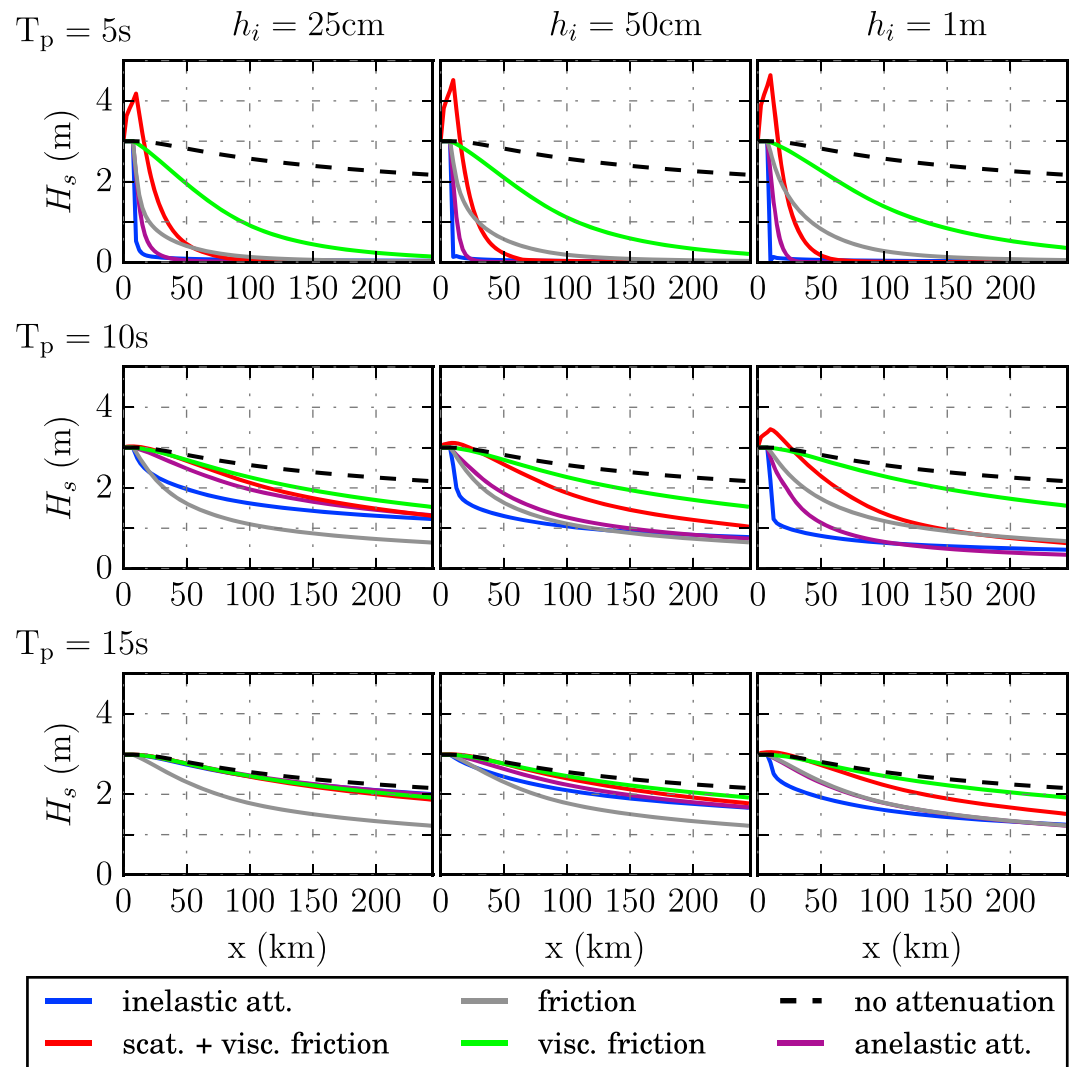


Figure 7. Distribution of H_s along the x direction at the center of the domain, for different peak periods ($T_p = 5, 10,$ and 15 s) and ice thickness ($h_i = 0.25, 0.5,$ and 1 m). Different colors correspond to the activation of different processes. The vertical dotted black line indicates the ice edge position.

from 10 to 70 km (see Figure 9). This setup roughly represents the ice conditions discussed by Collins et al. (2015). The ice thickness was taken constant over all the ice-covered area. Wave conditions at the forcing boundary are constant with a narrow Gaussian frequency spectrum centered around a fixed peak frequency f_{p_i} with a half width of 0.01 Hz.

The distribution of wave energy along the left boundary at $x = 0$ is also Gaussian with a half-width of 10 km and a maximum significant wave height of 3 m. The model was ran without wind input, wave breaking, or nonlinear source terms. Alternatively, the spectrum at the boundary was replaced by off-ice spectra provided by a realistic simulation of the Arctic using WAVEWATCH III (Stopa et al., 2016) and corresponding to the event of 2 and 3 May 2010, described by Collins et al. (2015). For that case, we rotated the forcing spectrum so that the direction with the largest density of wave energy was lined up with our x axis.

Figures 7 and 8 illustrate the effects of different processes on ice breakup and the associated wave height attenuation. Results are all presented after an equilibrium is reached (which takes ≈ 8 hr for the selected processes and their combinations).

As expected from the parameterizations, attenuation due to basal friction is slightly sensitive to the ice thickness due to the G factor and the dispersion relation and varies more strongly with the wave period,

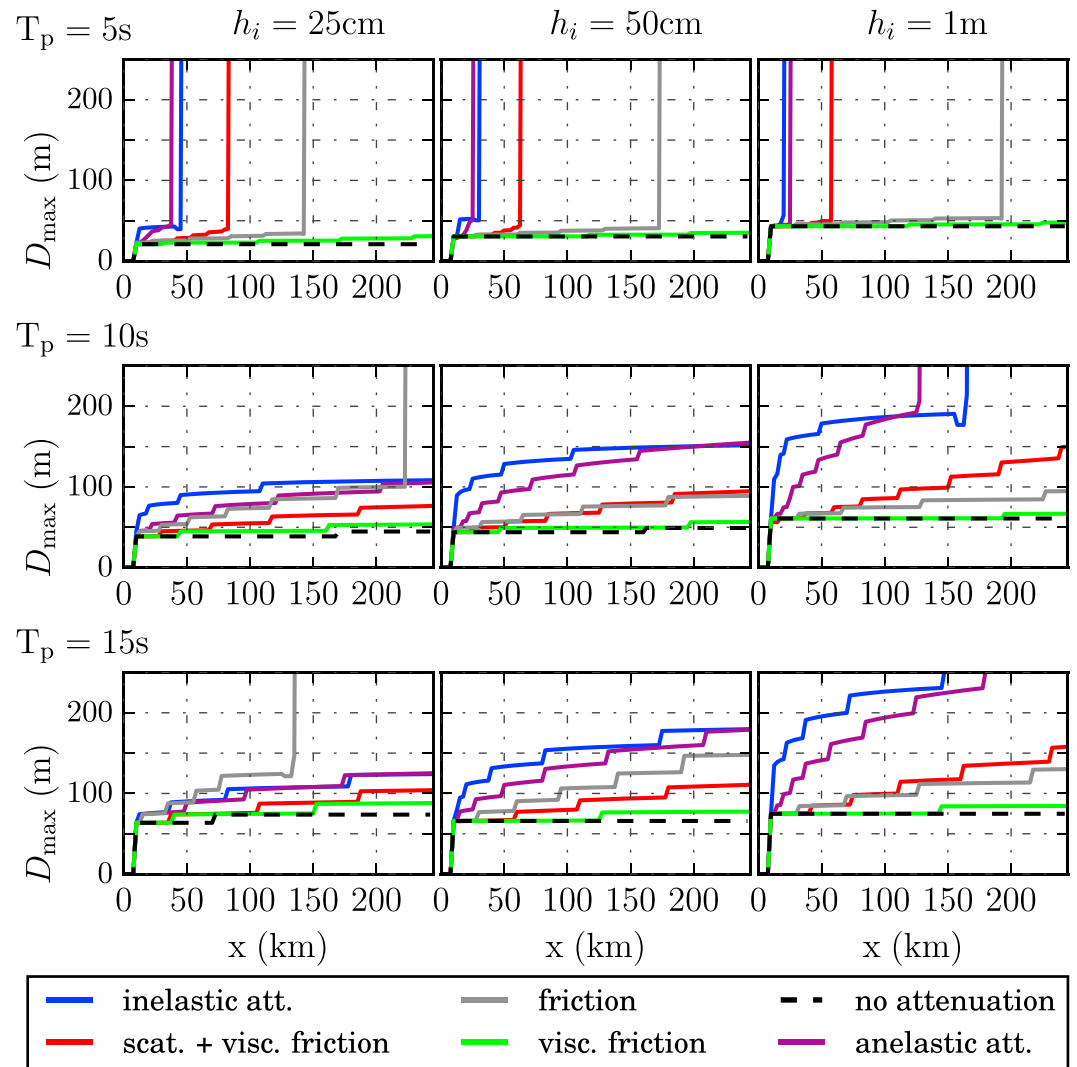


Figure 8. Distribution of D_{\max} along the x direction at the center of the domain, for different peak periods ($T_p = 5, 10,$ and 15 s) and ice thickness ($h_i = 0.25, 0.5,$ and 1 m). Different colors correspond to the activation of different processes.

Table 1

Values of the Attenuation Rates Supposing an Exponential Attenuation α (km^{-1}), and the Associated Determination Coefficient R^2 for Various Combination of Wave Period and Ice Thickness When Scattering and Viscous Friction Are Activated

Scattering + viscous friction	$D_{\max} < 100$ m		$D_{\max} > 100$ m	
	α	R^2	α	R^2
$T_p = 5$ s, $h_i = 25$ cm	0.049	0.99	0.008	0.98
$T_p = 10$ s, $h_i = 25$ cm	0.002	0.99	/	/
$T_p = 5$ s, $h_i = 1$ m	0.080	0.99	0.024	0.95
$T_p = 10$ s, $h_i = 1$ m	0.008	0.99	0.003	0.99

Note. The slash bars indicate that there for such combinations of wave period and ice thickness, there is no region for which $D_{\max} > 100$ m.

with a local dissipation rate proportional to k_i/\sqrt{T} that gives a decay distance proportional to $T^{-3.5}$. For waves longer than 10 s, the viscous dissipation (green curve, for which the turbulent term of the friction has been removed) is very weak, with only a 33% reduction in wave energy over 200 km for $T_p = 10$ s. A transition to turbulent dissipation, when this is allowed by the user and for a boundary layer Reynolds number of the order of 10^5 , typically increases the dissipation rate by up to a factor 10 when using a roughness length of 1 cm (Stopa et al., 2016; gray curve). In practice, this is only relevant near the ice edge for wave heights larger than 2 m in open water, because the Reynolds number is reduced as waves are.

When combined to basal friction only the breakup of relatively thin ice is not a monotonous function of the wave period, as shown with the gray lines in Figure 8 for $h_i = 0.25$ m: 10-s waves are more efficient for breaking the ice than 5- or 15-s waves. This comes from two competing effects.

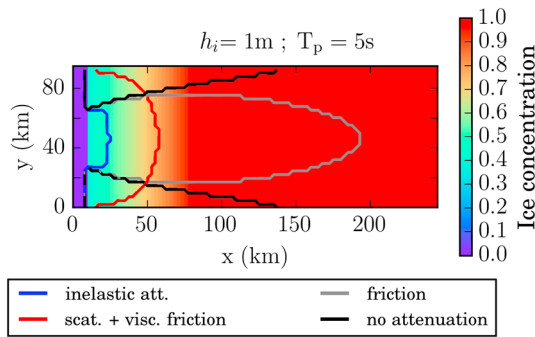


Figure 9. Representation of the idealized test domain. In the background is plotted the ice concentration. Waves radiate from the western boundary. Solid lines represent the contour $D_{\max} = 200$ m showing the extent of broken ice achieved for waves with $T_p = 5$ s and an ice thickness of 1 m with the activation of various processes.

On the one hand, the attenuation is weaker for longer waves, which allows the waves to penetrate further into the ice. On the other hand, longer waves are less steep and are thus less prone to breaking the ice.

We also note that thicker ice gives larger floes for $T_p = 5$ s, but this reverses for $T_p \geq 10$ s with thicker ice giving smaller floes. This is true for all attenuation processes and it is also explained by two competing effects. First, the wavelength λ_i is influenced by ice thickness, in particular for short periods like $T_p = 5$ s. Hence, thicker ice corresponds to less steep waves, reducing the ice breakup. Second, the maximum strain grows linearly with the ice thickness (see equation (14)). As a result, for a given wave height in ice-covered water, thick ice breaks more easily than thin ice (Figure 4). This second effect is dominant for larger periods.

Scattering alone does not dissipate energy, and energy grows with time with multiple scattering in the model domain, so that for $T_p \geq 10$ s, waves are able to break the ice cover on its entire length after a few weeks. We therefore chose to combine it with the weakest dissipative process

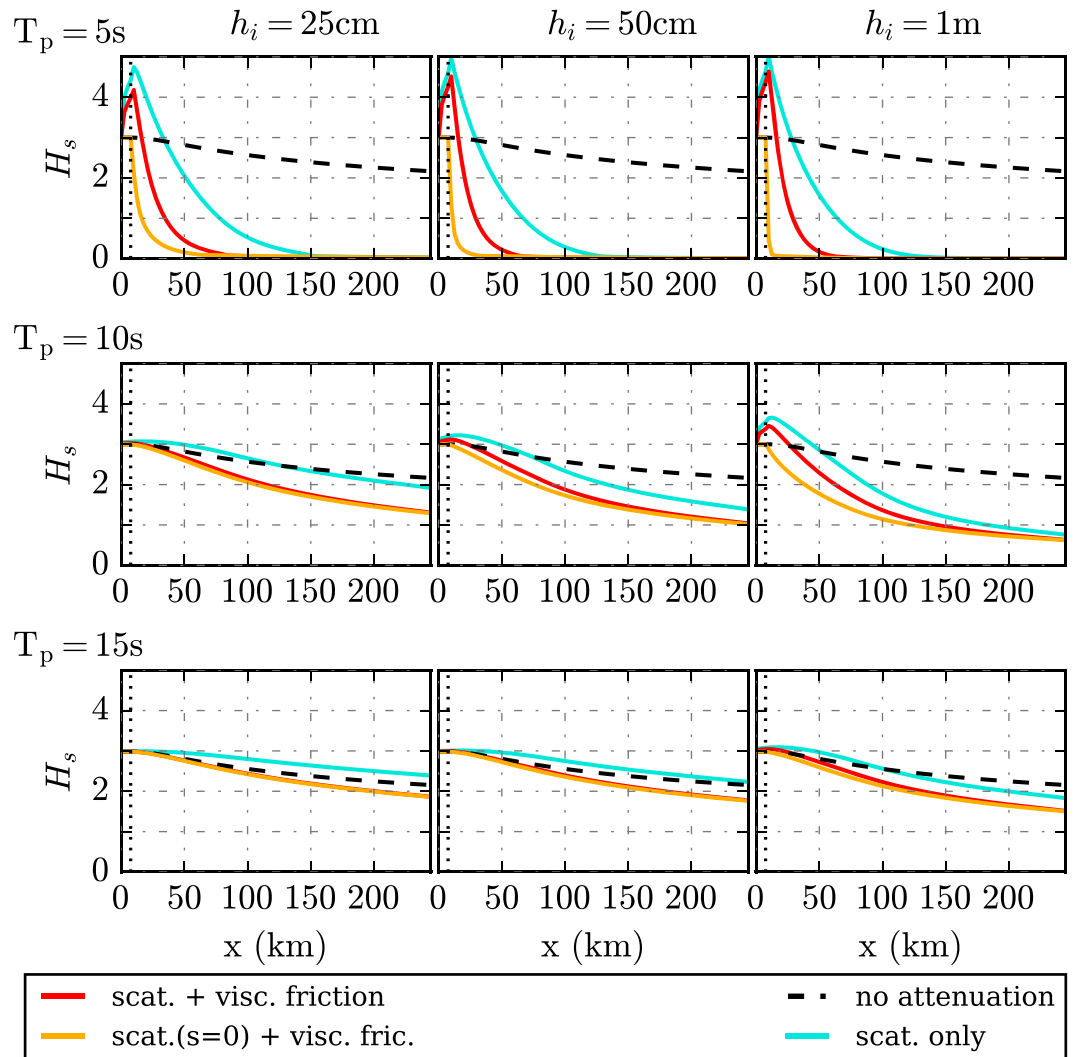


Figure 10. Distribution of H_s along the x direction at the center of the domain, for different peak periods ($T_p = 5, 10,$ and 15 s) and ice thickness ($h_i = 0.25, 0.5,$ and 1 m). Different colors correspond to the activation of the different processes that involve scattering. The vertical dotted black line indicates the ice edge position.

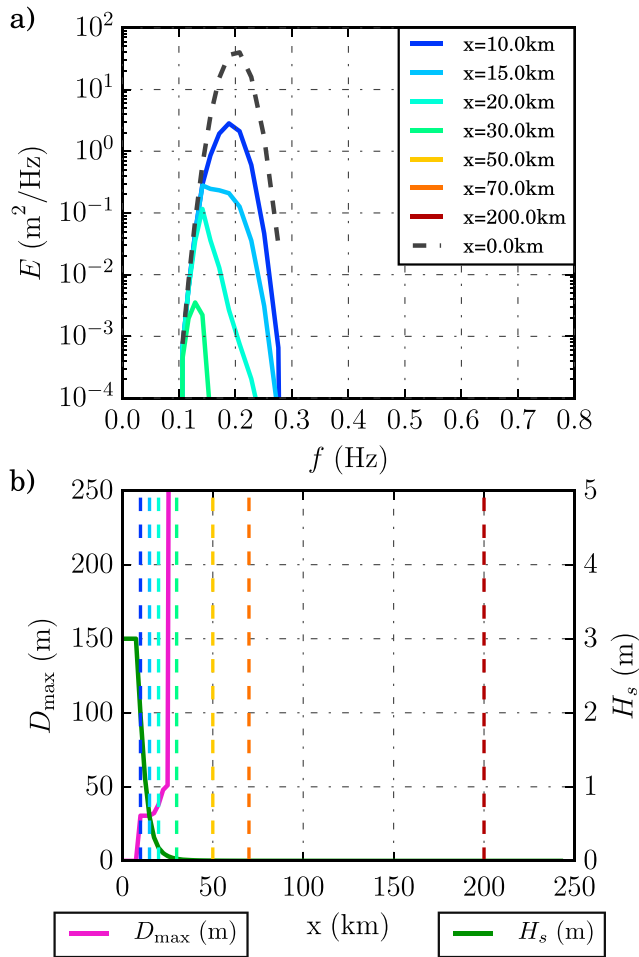


Figure 11. (a) Surface elevation spectra at various position along the x axis at $y = 45$ km, once a steady state is reached, using only anelastic attenuation. (b) Values of D_{max} and H_s along the x axis at $y = 45$ km. Each vertical dashed line represents the position at which is taken the spectrum of the associated color in (a). The ice thickness for this run is set constant to 50 cm and the incoming waves have a peak period $T_p = 5$ s.

ters. It prevents the ice from being broken in very small floes, since they result from the ice breakup induced by short waves. Anelastic attenuation is nevertheless strongly dependent on frequency: dissipation strongly decreases for long-period waves, to the point it almost vanishes for $T_p = 15$ s and $h_i = 0.25$ m. Figure 11a shows the wave elevation spectra for various position along the x direction at the center of the test domain. It suggests the existence of a cutoff frequency above which almost all the energy is dissipated. Figure 11b enables the comparison between the evolution of this cutoff frequency along the x direction and the evolution of the maximum floe size D_{max} . They show a parallel evolution that results from the F_λ factor presented in equation (17): as D_{max} increases, the cutoff frequency is shifted toward lower frequencies. Thus, ice breakup allows for long waves to penetrate further into the ice-covered sea.

Table 2

Values of Fitted Exponential Attenuation Rates α (With Units of km^{-1}), and the Associated Determination Coefficient R^2 for $T_p = 10$ s and $h_i = 50$ cm When Only Inelastic or Anelastic Attenuation Is Activated

$T_p = 10$ s, $h_i = 50$ cm	Anelastic		Inelastic	
	α	R^2	α	R^2
$D_{\text{max}} < 100$ m	0.009	0.99	0.048	0.91
$D_{\text{max}} > 100$ m	0.003	0.97	0.001	0.87

we had: the viscous friction. The results are shown in Figures 7 and 8. We observe that they differ significantly from the one achieved with viscous friction only, which indicates that scattering is the dominant process in this combination. Waves undergo a noticeable attenuation in the ice-covered ocean, which perceptibly increases with the ice thickness and the wave frequency. The reflected waves in the open sea prior to the ice edge lead to an increase of the wave height up to ≈ 2 m for $T_p = 5$ s. We fitted an exponential law to the spatial evolution of H_s evolution and summarized the results in Table 1. As expected, the effective attenuation along the x axis is exponential, with determination coefficients $R^2 > 0.95$ as long as there is no steep change in D_{max} . When the ice is broken, attenuation rates for waves with $T_p = 10$ s are found to be of the same order than the ones reported in Kohout et al. (2014) for $H_s < 3$ m in the Antarctic MIZ, when the attenuation is exponential. For $T_p = 5$ s, the order of magnitude of our attenuation rates is increased by a factor 10. When the ice is unbroken, the attenuation rates fall down along with the number of reflections. Figure 9 illustrates an other effect of scattering: an increase in the directional spread of waves which are reflected in all directions, resulting in a broadening of the beam of energy in the y direction. This broadening depends on α , and so increases along with ice thickness and decreases with the wave period. Removing the viscous part of the basal friction (see Figure 10) enhances the spread (not shown) and the increase of wave height at the ice edge, and waves are still attenuated as they propagate further into the ice. However, as raised by one of the reviewer, in the case of very long MIZ, without any dissipation process, the energy-conserving scattering produces unrealistic energy levels with a very weak decay far into the ice cover. Such unrealistic results are particularly pronounced in stationary conditions and highlight the importance of dissipation processes for producing realistic decays. Besides, for thin ice and waves longer than 15 s, the attenuation due to scattering becomes very weak and the addition of the low reflected energy to the incoming energy leads to a weaker decay of wave heights, and enhanced energy levels all along the domain. This latter observation and the increase of H_s at the ice edge are easily removed by setting $s_{\text{scat}} = 0$ (Williams et al., 2013b), which forces scattering to dissipate the waves but sacrifices energy conservation.

Anelastic attenuation gives a very strong attenuation of short waves, as the wave height falls down from 3 m to a few centimeters in a few kilometers. It prevents the ice from being broken in very small floes, since they result from the ice breakup induced by short waves. Anelastic attenuation is nevertheless strongly dependent on frequency: dissipation strongly decreases for long-period waves, to the point it almost vanishes for $T_p = 15$ s and $h_i = 0.25$ m. Figure 11a shows the wave elevation spectra for various position along the x direction at the center of the test domain. It suggests the existence of a cutoff frequency above which almost all the energy is dissipated. Figure 11b enables the comparison between the evolution of this cutoff frequency along the x direction and the evolution of the maximum floe size D_{max} . They show a parallel evolution that results from the F_λ factor presented in equation (17): as D_{max} increases, the cutoff frequency is shifted toward lower frequencies. Thus, ice breakup allows for long waves to penetrate further into the ice-covered sea.

The dependency on ice thickness is also important. It is illustrated by the fact that for $T_p \geq 10$ s, as opposed to friction, floe size tends to increase with ice thickness, meaning that the wave height attenuation strongly controls how the strain evolves.

Inelastic attenuation shows trends that are similar to the anelastic attenuation with some nuances: the nonlinearity of the process with the wave amplitude gives even stronger attenuation near the ice edge where

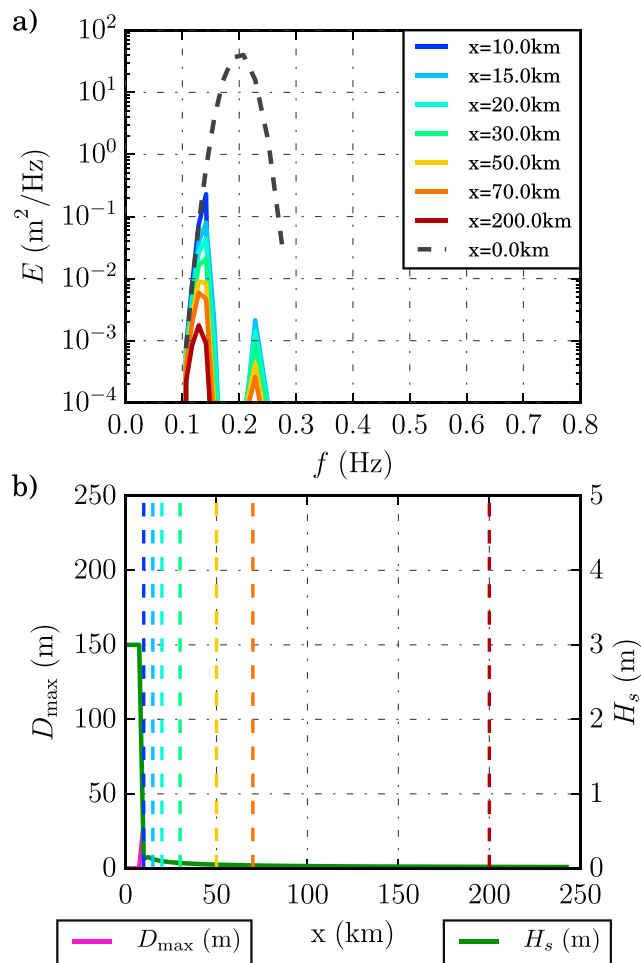


Figure 12. Same as Figure 11 for inelastic instead of anelastic dissipation.

the wave height is still large, and a lower dissipation rate further into the ice (see Table 2 and Figure 12). Once waves do not exceed a few centimeters in height, the strength of the inelastic dissipation is much reduced compared to anelastic effects, allowing waves to propagate further. This is shown in Figure 12a, for which the energy associated with $f \approx 0.22$ Hz is not dissipated much once the spectral density is below $5 \times 10^{-3} \text{ m}^2/\text{Hz}$. This leads to the presented bimodal spectrum into the ice, as waves with shorter wavelengths but lower wave heights end being less curved than longer waves with higher wave heights and therefore less quickly attenuated when the ice is flexed. It explains why the region with broken ice extends further with inelastic dissipation compared to anelastic dissipation (Figure 8).

4. Model Evaluation

In the previous section we have shown that unless it is scaled by ad hoc factors (e.g., Liu et al., 1991), anelastic and inelastic processes produce stronger attenuation than basal friction. Both are also very sensitive to ice floe size. For broken ice, the attenuation is dominated by under-ice friction for wave periods over 5 s, except in the case of very thick floes or if the wave height is too low to trigger turbulence. We now evaluate the effect of all processes and some combinations in several realistic conditions.

4.1. Svalbard Swell Event of 2 May 2010

Here we reproduce the conditions observed to the south of Svalbard on 2 and 3 May 2010, as described by Collins et al. (2015). They report a storm event in which the R/V Lance, initially trapped in the ice, encountered a sudden change in the waves and ice conditions. As it was blocked in ≈ 60 -cm-thick compact ice without feeling any wave, the vessel underwent a first wave train that started to break the ice. In about 1 hr, the ice got completely broken up into small floes (≈ 10 m) and the wave height reached about 3 m. We investigate here if such an event could be at least qualitatively reproduced by the processes we implemented in WAVEWATCH III.

Figure 13 shows the effects of the activation of each process on the wave attenuation and on the maximum floe size given the above-mentioned storm conditions applied at the western boundary of our simple domain. With scattering and friction, H_s decreases progressively as waves propagate into the ice. Except in the case of the full friction term with thin ice floes ($h_i = 25$ cm), the domain ends up entirely broken at the end of the simulation. Anelastic attenuation leads to stronger attenuation, especially near the ice where the high-frequency part of the wave spectrum is damped, but the attenuation remains relatively smooth throughout the domain. The increase in the ice thickness illustrates a positive feedback between the floe size and the attenuation: in thick ice, waves undergo a strong damping as soon as they reach the ice edge. This damping consequently limits the breakup of the ice, which in turn increases the attenuation.

Inelastic attenuation gives a different story. For very thin ice ($h_i = 25$ cm), short waves are strongly damped at the ice edge, which results in a substantial loss of energy. It prevents the ice from being broken in small floes, and as a consequence does not lead to break up similar to Collins et al. (2015) report. Nevertheless, in this latter paper, floes are reported to be 50- to 60-cm thick. In this case (Figures 13b and 13e), the domain can be divided into two parts:

1. The western part, with broken ice, weak attenuation and high H_s .
2. The eastern part, with unbroken ice, and low H_s .

Between these two parts, waves create a front characterized by strong gradients of D_{max} and H_s , which becomes narrower as the ice thickness increases (Figures 13c and 13f). Note that for the floe size, it exists a second front that corresponds to an initial fracture by long waves ($\lambda_i \approx 300$ m).

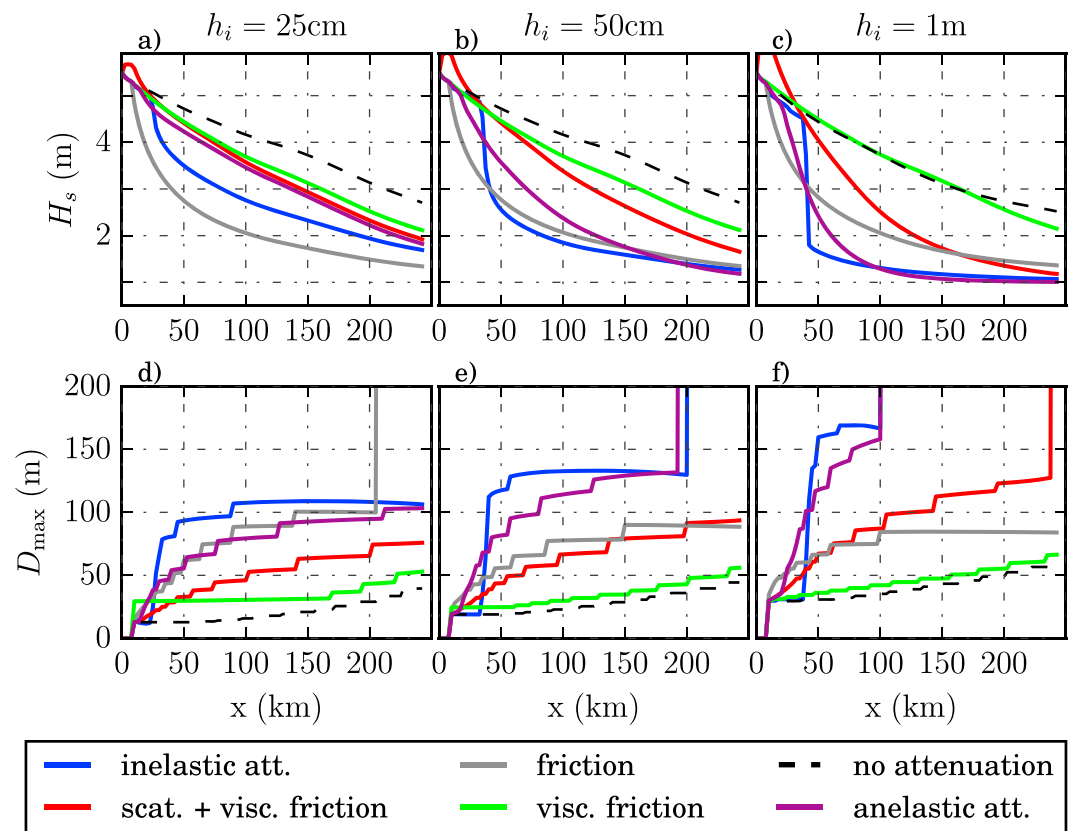


Figure 13. Distribution of H_s (top panel) and D_{max} (bottom panel) along the x direction at the center of domain, for different ice thickness ($h_i = 0.25, 0.5,$ and 1 m). Different colors correspond to the activation of different processes.

Figure 14 clarifies the interpretation of such results with the inelastic attenuation. The nonlinearity of this process allows the low energetic but high-frequency components of the wave spectrum to propagate without being dissipated in the first few kilometers. The curvature associated with these short waves leads to ice breakup into floes that are no longer bent by longer waves. Therefore, the energy associated with the dominant waves progresses into the ice cover until it reaches unbroken ice. This notwithstanding, the attenuation rates of the high-frequency waves are unexpectedly low compared to common knowledge.

Inelastic attenuation thus greatly depends on the value of C_λ . The observations made by Collins et al. (2015) can therefore be seen as an opportunity to discuss the values we chose for this latter parameter. Figure 15 shows both the spatial H_s profile after 12 hr as well as its temporal evolution at a given point of the domain, close to the front position. Increasing C_λ to 0.4 smoothes the transition, increasing H_s from 50 cm to 3 m in about 7.5 hr, and was therefore rejected. On the opposite, $C_\lambda \leq 0.2$ dissipates too much energy as soon as it encounters sea ice (top panel of Figure 15), while Collins et al. (2015) reported that there was almost no attenuation after the breakup occurred at the ship location (estimated to be $C_\lambda = 0.3$ seems to be a better choice as it reproduces a steep H_s increase from about 1 m to over 3 m in about 2 hr (bottom panel of Figure 15) and a relatively small drop of H_s at the ice edge.

The inelastic attenuation combined with viscous friction and scattering (Figure 16) has also been tested to see if the front still exists when processes that focus on short waves are added. To avoid getting too much dissipation, we also increased the value of B , the creep parameter, from 10^7 to 1.510^7 Pa.s^{1/3}. Such a change shifts the front position 15 km eastward and makes it visibly smoother. On the opposite, activating scattering and viscous friction shifts the front westward. Activating scattering actually moves the front to the ice edge, as the high frequencies are damped so much that the ice cannot be broken into small floes. Viscous friction does not modify much the results: the front moves 20 km westward and is slightly smoother while remains clearly visible, both for H_s and D_{max} . We can, however, suggest that in the event reported by Collins et al. (2015), floes are only a few meters wide and much smaller than the wavelength. Scattering may thus damp

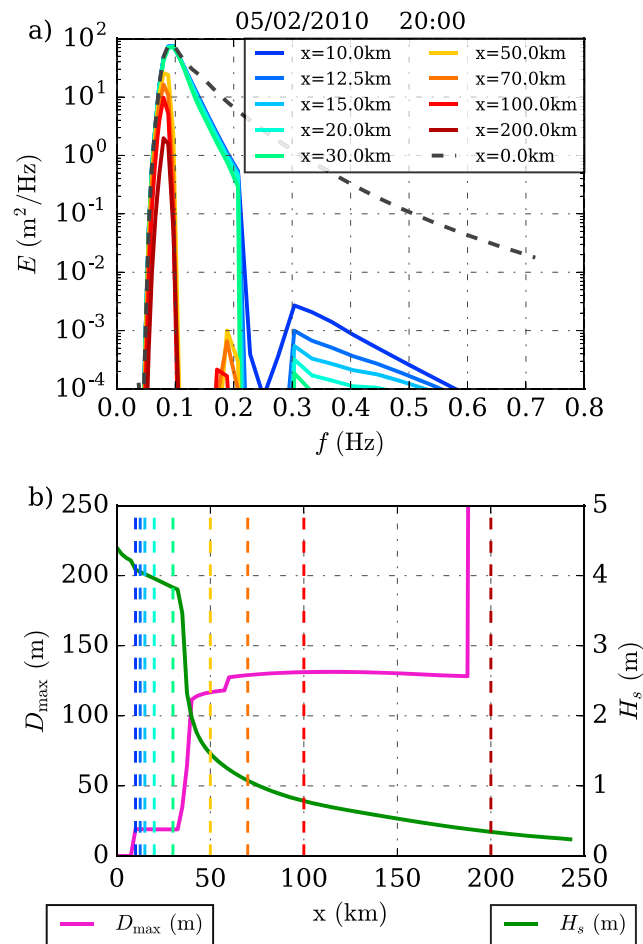


Figure 14. In (a), solid lines represent the wave spectra at various position along the x axis of the domain after the equilibrium has been reached when inelastic attenuation is activated. The spectra are taken at the center of the domain according to the y axis. The dashed line is the input spectrum at the western boundary which corresponds to the simulation of the storm event in the south of Svalbard on 2 May 2010. This input spectrum was computed by running WW3 on a 12.5-km resolution grid without any ice. In (b), the distribution of D_{max} and H_s along the x axis is plotted, while the colors of the vertical dashed lines refer to the position indicated in (a).

the short waves close to the front zone, as long as the floes are large enough not to be negligible compared to the wavelength, and then stops being efficient after the floe size is reduced to a few meters. This cannot happen in our model as it has been supposed that flexure is responsible for breaking the ice and that it exists a minimum size below which floes cannot result from flexural failure (Mellor, 1986).

4.2. A Realistic Model of the Arctic

We now run the model on a stereographic polar grid of the Northern Hemisphere at 12-km resolution (see Stopa et al., 2016, for details) with the ice concentration and thickness forced by the Arctic Ocean Physics Reanalysis (1991–2014) provided by Copernicus Marine Environment Monitoring Service (<http://marine.copernicus.eu>) and based on TOPAZ4 reanalysis products (Sakov et al., 2007). The model is forced by the 3-hourly ERA-Interim 10-m neutral winds (Dee et al., 2011). The source terms are those of Ardhuin et al. (2010). Initially, D_{max} is set to $D_{\text{max,init}} = 1,000$ m. To have a better insight of the Svalbard event mentioned above, a regular grid has been nested between $18^\circ \text{E}/27^\circ \text{E}$, and $76^\circ \text{N}/78^\circ \text{N}$, with a 3.2-km resolution. The period tested was May 2010.

Strong (2012) suggested that the MIZ could be defined as the ice-covered area with $0.15 < c < 0.8$ but also as the area of interactions between waves and sea ice (Dumont et al., 2011). As the ice concentration and thickness are given by the TOPAZ reanalysis product, the only ice parameter on which waves have an effect

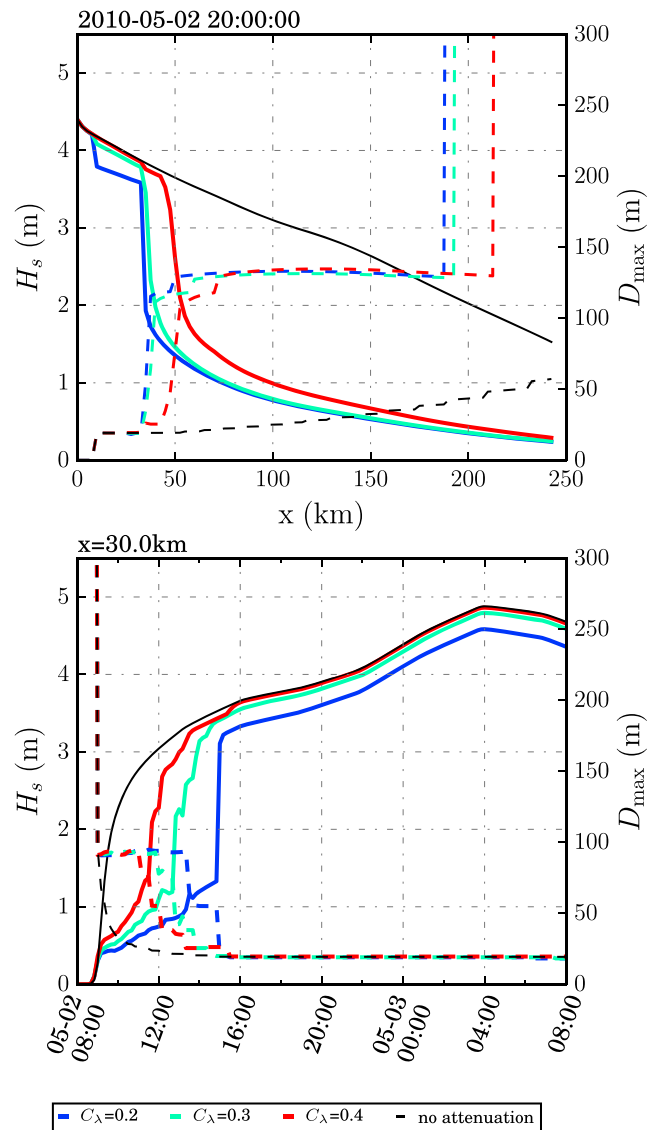


Figure 15. Evolution of H_s and D_{max} spatially (top) and temporally (bottom), at the center of the domain for the idealized test reproducing the Svalbard observation of 2 May 2010. The run starts at 8:00 a.m. on 2 May 2010. The temporal evolution is taken at $x = 30$ km (20 km from the ice edge). Each color represents a different tuning of C_λ .

is the ice diameter. In such conditions, we chose to define the MIZ as the area where ice has been broken by the waves, for example, for which $D_{max} < D_{max_{init}}$, and $c > 0.15$ to ensure a significant presence of ice.

In Figure 17, we present the MIZ areas achieved for each process and some combinations using the criterion mentioned above. The blue line represents the MIZ area when the model is run with only inelastic attenuation to dissipate the wave energy in the ice. As inelastic attenuation almost vanishes when the ice is broken, waves tend to penetrate further into the ice, which broadens the MIZ extent in a unrealistic way. As a consequence, inelastic attenuation only cannot explain the wave attenuation in the ice. It has to be associated with friction to avoid breaking the whole Arctic sea ice pack after the simulation has run for a few months. Note that scattering does not dissipate energy either, and consequently, a combination of this latter process and inelastic attenuation only is not suitable. Just like Williams et al. (2013a), we observe that the concentration criterion and the breaking criterion give different results for the boundary of the MIZ but with the same order of magnitude. The area we get when activating only viscous friction also shows peaks that correspond to unrealistically wide broken areas in the Arctic, due to the low dissipation rate it is associated with. Other processes and combinations are more realistic. The combination of scattering and viscous friction shows very

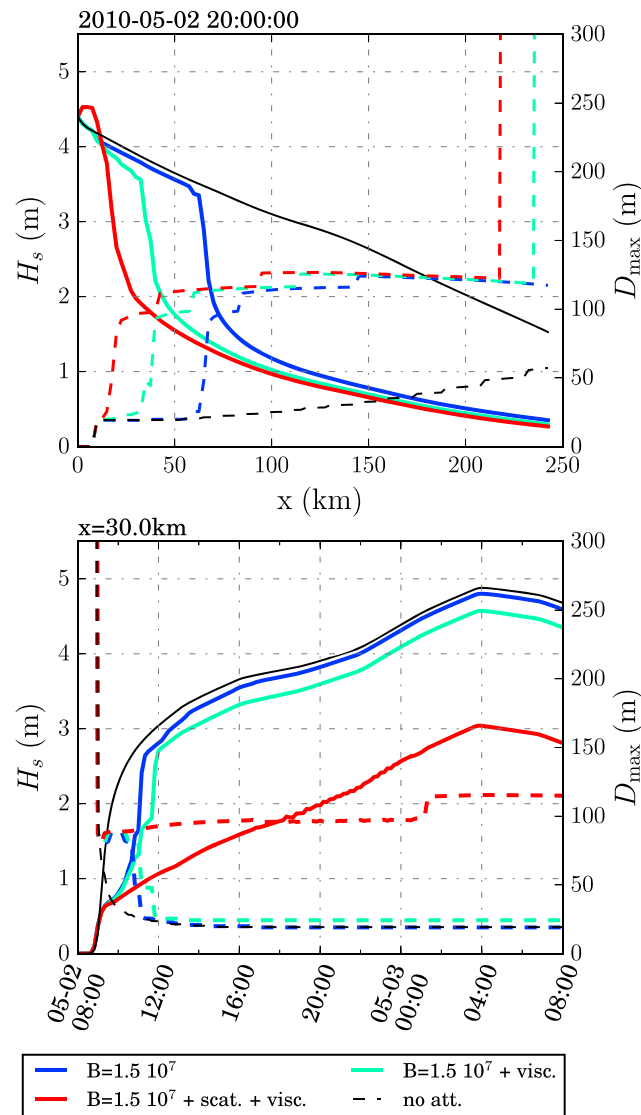


Figure 16. Evolution of H_s and D_{max} spatially (top panel) and temporally (bottom panel), at the center of the domain for the idealized test reproducing the Svalbard observation of 2 May 2010. The run starts at 8:00 a.m. on 2 May 2010. The temporal evolution is taken at $x = 30$ km (20 km from the ice edge). Each color represents a different combination of processes.

similar behavior to the whole friction term, giving areas of the same order of magnitude as the results achieved with the Strong (2012) concentration criterion. Comparatively, adding the inelastic attenuation to this combination gives areas roughly twice as low, stressing the important impact of the inelastic dissipation. The activation of anelastic attenuation gives about the same area as all the previous processes combined, emphasizing the very high attenuation our parametrization gives for this mechanism.

The geographical representation of the MIZ on a pan-Arctic scale is shown in Figure 18 for two combinations of attenuation processes: on the one hand, inelastic attenuation, scattering and friction and on the other hand scattering and viscous friction. The snapshot is taken during the storm event on Svalbard. The MIZ extent in all the Barents sea appears larger than in other regions, such as eastern Greenland. In calm conditions, MIZ extents in these two regions are quite similar. As an order of magnitude, the averaged extent of the MIZ according to the breaking criterion in the region between southeastern Greenland to north Svalbard in Figure 18 is 40 km with all processes activated, and 80 km with the scattering/viscous friction combination. In the Barents sea, and in particular in the eastern part of Svalbard, the MIZ exceeds 120 km with all processes activated, and 200 km with scattering and viscous friction activated.

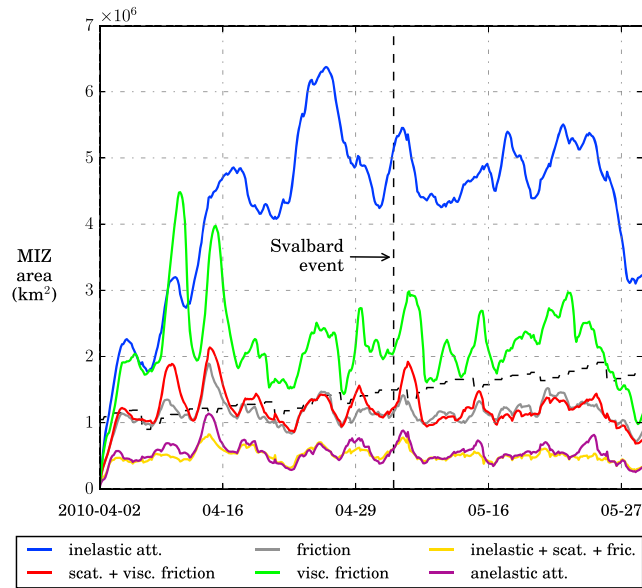


Figure 17. The Marginal Ice Zone (MIZ) area for various processes as computed in April–May 2010. The MIZ is defined as the region for which $c > 0$ and $D_{\max} < 1,000$ m. The dashed black line represents the MIZ area according to the criterion given by $0.15 < c < 0.8$.

In Figure 19, inelastic attenuation, scattering, and basal viscous friction have been combined. As the ice thickness given by TOPAZ4 did not agree with Collins observations, we set the ice thickness constant to 50 cm over all the domain. At 18:00 a.m. on 2 May 2010, the ice is already broken into relatively small floes at the ship position, located in close drift ice ($c < 0.8$ and $D_{\max} \approx 60$ m). The sea state varies rapidly between 18:00 and 00:00:00 on 3 May 2010 ($H_s \approx 1$ m).

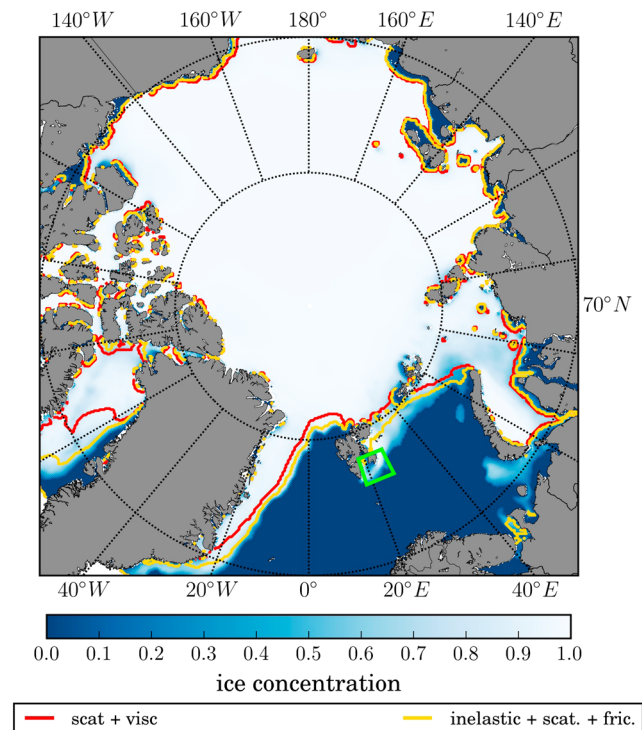


Figure 18. $D_{\max} < 1,000$ -m contour for two different combinations of processes on 3 May 2010, at 00:00. The green square delimits the area represented in Figure 19.

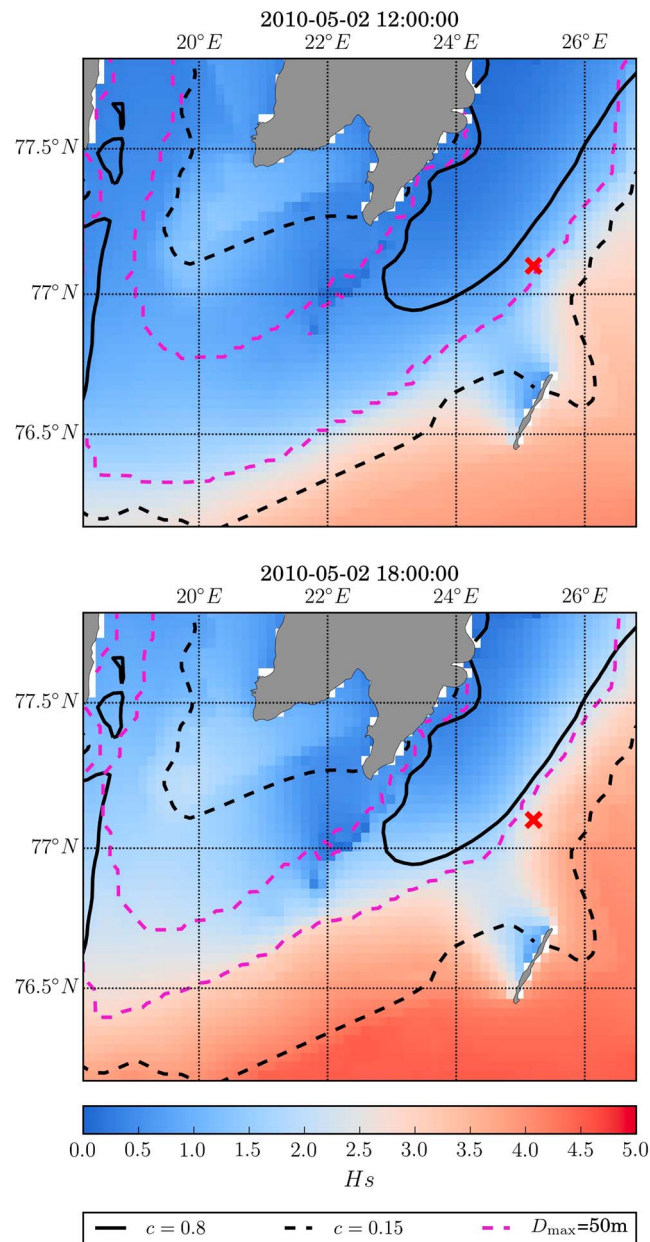


Figure 19. $D_{\max} = 50$ m, and ice concentration $c = 0.8$ and $c = 0.15$ contours are plotted over H_s distribution in Svalbard on 2 May 2010, before (top panel) and during the storm (bottom panel). The red x represents the location of R/V Lance where observation is available (Collins et al., 2015). For this model simulation, three attenuation (inelastic, viscous basal friction, and scattering) processes have been combined.

The border between floes with $D_{\max} \approx 60$ m and floes broken by the swell event with $D_{\max} \leq 30$ m nevertheless reaches the R/V Lance location between 12:00 and 18:00 in our simulation. It is associated with an important change in wave height similarly to the previous results in the idealized tests. Adding the turbulent term to the friction process prevents the ice from being broken far enough to reach the boat. However, reducing the roughness length for basal friction or the inelastic dissipation parameter B can affect the results significantly, in particular the spatial extent of ice breakup and H_s values at the location of R/V Lance. This simulation therefore stresses again the high dependency of our physical parameterizations on a number of parameters. That would require attention in future in situ investigations.

5. Discussion

The observed nonlinear behavior of wave attenuation when ice is broken is generally consistent with the expected effects of inelastic attenuation, and pan-Arctic simulations of ice attenuation and breakup appear reasonable when combining under-ice friction and inelastic attenuation. These results have to be mitigated since the spectra achieved with inelastic attenuation do not really look like the ones measured by Collins et al. (2015) in Figure 3. They indeed lack the very sharp decrease around 0.2 Hz that we observe in Figure 14. It might be that the frequency range of the spectra presented in Collins et al. (2015) is not wide enough or that the floes were so small when the spectra were measured that there was no ice flexure anymore. It is also possible that our inelastic attenuation parametrization reproduces the event successfully without being the real process behind the sudden change in wave height. Furthermore, the existence of short waves far into the ice, even associated with very low energy levels, is very unlikely and stresses the necessity to combine inelastic attenuation with other processes.

A convincing validation of the inelastic attenuation process would require a variety of cases with accurate observations of the evolution of ice properties (floe size, thickness, and concentration ...) during a wave event. The existence of a cutoff frequency of the energy depending on the floe size could be investigated. Besides, the creep parameter B is very sensitive to the thickness and temperature of the ice (e.g., Cole et al., 1998), and here we have used an approximation that matches the estimations of Wadhams et al. (2011). It is also coherent with the suggestion by Cole et al. (1998) for the computation of the viscous creep, taking the value at the freezing point. Knowing that B is at its maximum for this temperature, we may have overestimated the inelastic attenuation. Likewise, the use of the mean ice thickness certainly leads to an underestimation of the wave dissipation.

Besides, inelastic deformation is expected to occur in large floes or unbroken ice areas and therefore does not explain wave attenuation reported in the first kilometers of the MIZ (Wadhams et al., 1986). Latter cases could be explained by scattering, friction, floe-floe collisions, slamming (Bennetts et al., 2015), and overflow (Toffoli et al., 2015), but their respective magnitude remains to be quantified in real conditions. These first kilometers of the MIZ, where we expect to find rather small floes, are also likely not compatible with the use of our dispersion relation, which hypothesizes a thin semi-infinite elastic ice plate. The choice of the dispersion relation can be important for a wave-in-ice model, and no theory has been successful in representing the wave behavior in a variety of ice conditions so far (Collins et al., 2017). Our choice should only be valid for unbroken large floes or packed ice, and we nevertheless extended it to the whole MIZ. The study of Sutherland and Rabault (2016) in particular suggests that the ice, once broken, loses its elasticity and that the dispersion relation tends toward the one in open water. This is, to our knowledge, one of the main limits of concerning the consistence of our model.

Anelastic attenuation is quite similar to the inelastic attenuation, with a cutoff frequency above which the waves are attenuated in the order of a few kilometers. The difference lies in the fact that this attenuation does not vary with the wave amplitude, which results in the strong damping of the shortest waves and the impossibility for the ice to be broken into small floes. Our conclusion is that our parametrization cannot reproduce case like described in Collins et al. (2015). This result may be due to the application of a parametrization that does not include the effects of the variety of ice conditions (ice temperature, ice brine, ice fatigue, ice thickness distribution, effective stress applied during the flexure ...) which can significantly impact the anelastic behavior of the ice.

Although our scattering model is strongly simplified, with isotropic energy redistribution, it is generally consistent with Wadhams et al. (1986) observations of the spectrum widening within the ice-covered sea. Such an increase in directional spread has not been observed in SAR imagery of waves with periods longer than 8 s (Ardhuin et al., 2017). This is consistent with the limited effect of scattering found when using the approach of Bennetts and Squire (2012). Our choice to redistribute the energy isotropically is certainly very imperfect, but it has the advantage to ensure the energy conservation without making scattering a dissipative mechanism. We are, however, aware that the scattering from an ice floe is actually far from uniform in all directions (Meylan, 2002; Sutherland & Rabault, 2016). A better solution could be to test the implementation of the full solution of 3-D scattering, even with simplified problems like for circular floes (Pete et al., 2004). Moreover, as Wadhams et al. (1988) point out, there is also a possibility that an incident wave scatters energy at different frequencies, typically harmonics of that frequency generated as floes are pitching and heaving, that can rapidly be dissipated. That would explain the absence of observed increase in directional spread with SAR imagery.

When combined with inelastic attenuation, scattering leads to prevent the ice from being broken, which does not allow the wave height front to progress into the MIZ. Collins et al. (2015), however, describes floes that are far smaller than the wave wavelengths. In these conditions, it might be that scattering simply vanished and let the waves to propagate freely. As mentioned above, our ice breaking parametrization does not allow for the floe size to take values lower than the minimum size given by the flexural failure theory (Mellor, 1986). This fact, added to the poor knowledge of the internal behavior of ice submitted to wave flexure, emphasizes the need for a better understanding of the ice rheology.

Scattering could very well dominate for shorter wave periods within the first kilometers of the sea ice cover as long as the ice is broken. Inelastic attenuation is a plausible candidate to explain the wave attenuation in unbroken packed ice. Some other dissipation mechanism, like friction below the ice, is an indispensable companion to inelastic attenuation, without which the wave amplitude would keep unrealistically large values (5 cm or more) where the amplitude is too low to produce a significant inelastic dissipation. We also suppose that scattering may prevent the short waves to penetrate far in the packed ice. The attenuation computed in our model results in a damping of the high waves, which although turbulence below the ice layer is expected, our formulation did not yield convincing results. Unfortunately, the roughness length for the wave motion is a sensitive but poorly known parameter. From our study, it appears that choosing a value 1 cm leads to consequent attenuation in the case of large wave heights, independently from the size of the floes. Such behavior is not compatible with cases where high waves are reported far into the ice cover (Collins et al., 2015; Kohout et al., 2014). We suspect that turbulence is reduced when the ice is broken as the floes may be able to follow at least a fraction of the horizontal water motions.

Our simulation of the case presented by Collins et al. (2015) suggests that dissipation within the ice layer may be important source of swell dissipation, and the expected strain rates could be associated with dislocations and a possible nonlinear strain-stress relationship (Cole & Durell, 2001). Such a relationship can explain the transition from strong attenuation in unbroken ice to little attenuation in broken ice. Hence, a knowledge of the floe size is necessary to analyze wave attenuation, but these results are not easily compared to other results without running a wave model in many different cases. For example, Meylan et al. (2014) report that long swells ($T_p=15$ s) in Antarctica have an attenuation consistent with a linear dissipation with $\alpha \propto T^{-2}$, in a case with floe diameters of the order of 20 m at most. None of the processes investigated here can reproduce this attenuation law, in particular basal friction has $\alpha \propto T^{-n}$ with $n = 3.5$ for viscous friction and larger values when turbulence is taken into account. Possibly, these attenuation rates estimated from the ratio of wave heights at two measurement locations are the result of a variable attenuation along the propagation. They may also have been contaminated by local wind-generated waves (Li et al., 2015).

6. Conclusion

The effect of sea ice on ocean waves, including the influence of floe sizes, has been implemented in the spectral wave model WAVEWATCH III, following the previous developments of Dumont et al. (2011) and Williams et al. (2013b) with monochromatic waves. These include the update of the floe size at each wave model time step depending on the ocean wave properties. Because scattering, anelastic attenuation, and inelastic attenuation are strongly dependent on floe sizes, the ice breakup introduces a feedback on the wave field with different evolution patterns.

Scattering does not dissipate energy but is effective when it comes to attenuate short periods in the first kilometers of the MIZ. In our model, scattering also leads to an increase in wave height and directional spread as documented by Wadhams et al. (1986). This increase in wave height can lead to more breakup of the ice cover. When combined with dissipation, the fact that scatter increases the average effective propagation time across a given region (see the diffuse arrivals in Figure 3 of Ardhuin et al., 2016) leads to a stronger attenuation.

In the cases of anelastic and inelastic effects, we have assumed that when the ice is broken, significant dissipation only occurs for floes larger than 0.3 times the wavelength. Anelastic attenuation gives the strongest dissipation of all the processes, especially near the ice edge. This strong attenuation makes it impossible for the shorter wave components to penetrate in the ice and contribute to its breakup. Such a strong attenuation is not compatible with high waves reported far into the ice cover. It could be partly explained by the variability of the activation energy for temperatures above -5°C (Cole, 1995). We indeed did not account for the temperature variation along the ice thickness profile, although the bottom part of sea ice, in contact

with the sea, is at the melting point $\simeq -2^\circ\text{C}$. Considering the high dependency on the activation energy value of this process, it may lead to overestimate the energy dissipation.

Inelastic attenuation produces a dissipation that is strongest for high waves and unbroken ice, during the cyclic flexure of the ice, but allows for waves to propagate in broken ice given that waves with intermediate frequencies have amplitudes small enough not to be dissipated and large enough to break up the ice. Such a transition from a strong dissipation to no dissipation can explain the qualitative behavior reported in Collins et al. (2015). Our simulations suggest that scattering and inelastic attenuation are not enough and that other dissipation processes are necessary to provide a strong enough background dissipation. A plausible mechanism is basal friction. The laminar-turbulent transition proposed by Stopa et al. (2016) produces high dissipation rates for high waves, which appear too large for the case of Collins et al. (2015).

Our model results show the importance of several possible feedback mechanisms between the floe size and the attenuation of waves, in particular anelastic or inelastic dissipation. The sensitivity of these effects on ice temperature calls for more validation studies and experiments on the mechanical properties of sea ice at small scales. Future studies with coupled waves and ice models will make it easier to investigate the effects of ice temperature and floe size distribution in real conditions.

Appendix A: Implementation of Scattering and Implicit Integration

Because the attenuation and scattering in the ice can be very strong, it is convenient to perform a separate integration of the ice terms $S_{\text{ice}} = S_{\text{id}} + S_{\text{is}}$. This combines a dissipation term

$$S_{\text{id}}/\sigma = \beta_{\text{id}}N, \quad (\text{A1})$$

and a scattering term which is of the form

$$\frac{S_{\text{is}}(k, \theta)}{\sigma} = \int_0^{2\pi} \beta_{\text{is}}(\theta - \theta') [N(k, \theta') - N(k, \theta)] d\theta', \quad (\text{A2})$$

in which the scattering coefficient β_{is} is a priori a function of the difference in direction between incident θ' and scattered θ directions, as well as the shape of ice floes. In general, the directional spectrum $N(k, \cdot)$ is a vector with N_{TH} (number of directions) components, and the source term is a vector of the same size given by the matrix product $S/\sigma = MN(k, \cdot)$ where M is a positive symmetric square N_{TH} by N_{TH} matrix with components given from the β_{id} values. The matrix M is easily diagonalized as

$$M = VDVT, \quad (\text{A3})$$

where D is a diagonal matrix containing all eigenvalues and V is the array of eigenvectors, and V^T is its transpose. As a result the split wave action equation for ice source terms

$$\frac{\partial N}{\partial t c_g} = \frac{S_{\text{id}}}{\sigma c_g}, \quad (\text{A4})$$

can be rewritten for the action N_i of each eigenvector V_i with eigenvalue λ_i , as

$$\frac{\partial N_i}{\partial t c_g} = \frac{\beta_{\text{id}} + \lambda_i}{\sigma c_g} N_i, \quad (\text{A5})$$

which has the following exact solution

$$N_i(t + \Delta t_g) = N_i(t) \exp [(\beta_{\text{id}} + \lambda_i)\Delta t_g]. \quad (\text{A6})$$

In all cases the eigenvector corresponding to an isotropic spectrum has an eigenvalue $\lambda_i = \beta_{\text{id}}$. In the case of an isotropic backscatter, β_{is} is a constant and the other eigenvalues are all equal to $(\beta_{\text{id}} + \beta_{\text{is}})$. This decomposition over the two eigenspaces simplifies the solution to

$$N(t + \Delta t_g) = \exp(\beta_{\text{id}}\Delta t_g)\bar{N}(t) + \exp[(\beta_{\text{id}} + \beta_{\text{is}})\Delta t_g] [N(t) - \bar{N}(t)], \quad (\text{A7})$$

where \bar{N} is the average over all directions. As a result, for a spatially homogeneous field, the spectrum exponentially tends to isotropy over a time scale $1/(\beta_{\text{id}})$.

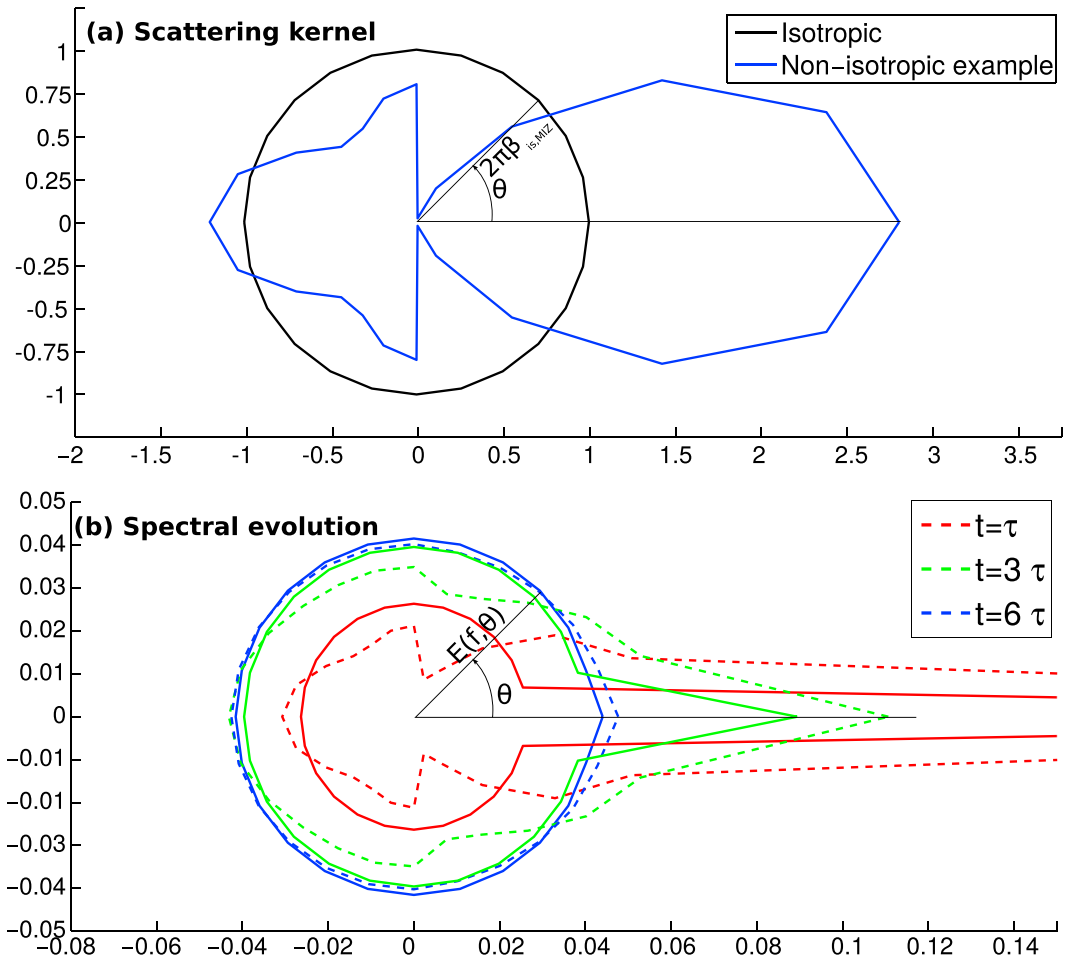


Figure A1. (a) Polar plots of possible shapes of the scattering kernel. (b) Time evolution of a directional spectrum that is spatially uniform and initially only in the $\theta_0 = 0$ direction, with $E(\theta_0) = 1/N_\theta$ using the isotropic (solid) or nonisotropic (dashed) scattering. We have used a scattering time scale $\tau = 1/(2\pi\beta_{is,MIZ})$.

Figure A1 shows an example with a nonisotropic scattering term resembling the one shown in Figure 12 of Masson and LeBlond (1989). For weak scattering or small time scales the spectral evolution can be significantly different between the two scattering terms. However, for large time scales or strong scattering the spectrum tends to isotropy.

Appendix B: Inelastic Dissipation for Random Waves

Using the flow law for ice given by Glen (1955), Wadhams (1973) expressed the energy dissipation rate per unit surface in a thin elastic plate of sea ice as the integral of the volumetric dissipation across the plate,

$$\frac{dE_t}{dt} = \int_0^{h_i} |\sigma_{xx}^4 / (2B)^3| dz. \quad (B1)$$

We note that in Wadhams (1973), the ice thickness is $2h_i$. From this expression, Wadhams (1973) derived that in the case of a monochromatic wave (with height $H_i = 2a_i$ in the ice), the evolution of the wave height

$$\frac{d\langle (H_i/2)^2 \rangle / 2}{dx} = -\frac{Kh_i^5 I_3}{32\lambda_i^8 C_g G \rho g} \langle (H_i/2)^4 \rangle \quad (B2)$$

with

$$K = \frac{[Y^* k^2 / (1 - \nu^2)]^4}{5(2B)^3} \quad (B3)$$

$$I_3 = \frac{1}{\pi} \int_0^\pi \sin^4 \beta d\beta = 3/8. \quad (B4)$$

Assuming a random sea state with a Rayleigh distribution, we can linearize the dissipation rate,

$$\frac{dE_t}{dt} = -\alpha_{ine} E_{ice}. \quad (B5)$$

We note that for the Rayleigh distribution we have

$$\langle (H_i/2)^4 \rangle = 2 \left(\frac{H_{rms,i}}{2} \right)^4 = 2(2E_{ice})^2, \quad (B6)$$

which gives

$$\alpha_{ine} = \frac{8}{32 \times 5} C_g \frac{Kh_i^5 I_3}{\lambda_i^4 C_g G \rho g} \times \frac{E_{ice} k^4}{(2\pi)^4} \quad (B7)$$

Replacing $E_{ice} k^4 / (2\pi)^4$ by the curvature of dominant waves (see section 2.3), we finally get

$$\alpha_{ine} = \frac{3}{160} \left(\frac{Y^*}{2B(1 - \nu^2)} \right)^4 \frac{h_i^5}{\lambda_i^4 G \rho g} \times \left(\frac{C_g}{GC_{g,i}} \right) \int_{0.7k_i}^{1.3k_i} k_i^4 \omega N(k) dk \quad (B8)$$

Finally, in β_{ine} , we multiply α_{ine} by F_λ given by equation (17), which is a heuristic smooth transition from unbroken to broken ice, so that the dissipation gradually goes to 0 for waves much longer than the floe sizes, because in that case the ice does not deform and so does not dissipate wave energy.

Appendix C: Anelastic Attenuation for Random Waves

The area A_{loop} of the hysteresis loop of a viscoelastic material (as shown in Figure 5) actually represents the dissipated energy into heat during the cyclic loading. It follows that under cyclic loading at a frequency f for which we have

$$A_{loop} = 2 \int_0^{1/(2f)} \dot{\sigma} \epsilon dt, \quad (C1)$$

the time-averaged dissipation rate per unit volume W in Watts per meter cubed is therefore

$$W = A_{loop} f = 2f \int_0^{1/(2f)} \epsilon \dot{\sigma} dt \quad (C2)$$

where σ is the stress and ϵ is the strain of the deformation.

With a sinusoidal stress with radian frequency $\omega = 2\pi f$, $\sigma = \sigma_0 \sin(\omega t)$, the anelastic part of the strain is

$$\epsilon_{anelastic} = \sigma_0 (A_1 \sin(\omega t) \cos(\omega t) + A_2 \sin^2(\omega t)) \quad (C3)$$

With

$$A_1 = \alpha_d \delta D^d \frac{1}{\exp(\alpha_d s) + \exp(-\alpha_d s)}$$

$$A_2 = \delta D^d$$

in which terms are detailed in Table C1. The associated values have been extracted from Cole et al. (1998). Here we neglect grain-boundary relaxation process that are more relevant for higher frequencies.

Table C1
Parameters Used in Anelastic Attenuation Computation (See Cole et al., 1998, for Details)

Symbol	Quantity	Value
δD^d	Relaxation of dislocation compliance	$\Delta_d \Omega b^2 / K$ (Pa ⁻¹)
Δ_d	Dislocation density	1.8×10^9 (m ⁻²)
K	Restoring stress term	0.07 (Pa)
Ω	Orientation factor	π^{-1}
b	Burgers vector	4.52×10^{-10} (m)
B	Drag term	$B(T_K) = B_0 \exp(Q_v / (k_B T_K))$ (Pa s)
B_0	—	1.205×10^{-9} (Pa s)
k_B	Boltzmann constant	8.617×10^{-5} (eV/K)
Q_v	Activation energy	0.55 (eV)
α_d	Peak broadening term	0.54
s	Reduced variable	$\log(\tau \omega)$
τ	Relaxation time of the dislocation process	B/K (s)

Note. T_K is the sea ice temperature in Kelvin.

As a result the average dissipation rate is

$$W = 2 \frac{\omega^2}{2\pi} \sigma_0^2 \left(A_1 \int_0^{\pi/(\omega)} \cos^2(\omega t) \sin(\omega t) dt + A_2 \int_0^{\pi/(\omega)} \cos(\omega t) \sin^2(\omega t) dt \right) \quad (C4)$$

$$= \frac{4}{3} f A_1 \sigma_0^2 \quad (C5)$$

Assuming that the deformation is mainly elastic, we have

$$\epsilon \simeq \epsilon_{\text{elastic}} = \frac{z}{2} \frac{\partial^2 a_i}{\partial x^2} \quad (C6)$$

$$\sigma = \frac{\epsilon Y^*}{(1 - \nu^2)}. \quad (C7)$$

We thus have W as a function of z . Wadhams (1973) has shown that when $W(z)$ is integrated over an ice layer of thickness h_i ,

$$\rho g G \frac{dE_t}{dt} = 2A \left(k^2 \frac{Y^*}{1 - \nu^2} \right)^2 \langle a_i^2 \rangle \frac{(h_i/2)^3}{3} \quad (C8)$$

where $A = \frac{4}{3} A_1 \omega$. This gives

$$\frac{dE_t}{dt} = 2A \left(k^2 \frac{Y^*}{(1 - \nu^2) \rho g G} \right)^2 \langle a_i^2 \rangle \frac{(h_i/2)^3}{3} \quad (C9)$$

and substituting with

$$\langle a_i^2 \rangle = \left\langle \left(\frac{H_i}{2} \right)^2 \right\rangle = \frac{H_{\text{rms}}^2}{4} = 2E_{\text{ice}} = 2 \frac{C_g}{GC_{g,i}} E_t \quad (C10)$$

It results the following source term β ,

$$\beta_{\text{anelastic}} = 4A \left(k^2 \frac{Y^*}{(1 - \nu^2) \rho g G} \right)^2 \frac{h_i^3}{24} \frac{C_g}{GC_{g,i}} \times F_\lambda \quad (C11)$$

in which F_λ is the heuristic smooth transition detailed in equation (17).

Acknowledgments

G. B. and F. A. are supported by DGA, ANR grants ANR-14-CE01-0012 MIMOSA and ANR-10-LABX-19-01, EU-FP7 project SWARP under grant agreement 607476, and ONR grant N0001416WX01117. C. S. and D. D. are funded by the Canadian Networks of Centers of Excellence ArcticNet and MEOPAR. This work has been carried out as part of the Copernicus Marine Environment Monitoring Service (CMEMS) ArcticMix project. CMEMS is implemented by Mercator Ocean in the framework of a delegation agreement with the European Union. Numerical model results are available at ftp://ftp.ifremer.fr/ifremer/www3/COM/PAPERS/2018_BOUTIN_ETAL. We thank the two anonymous reviewers whose comments and suggestions helped strengthen our analysis.

References

- Ardhuin, F., Chapron, B., Collard, F., Smith, M., Stopa, J., Thomson, J., et al. (2017). Measuring ocean waves in sea ice using sar imagery: A quasi-deterministic approach evaluated with sentinel-1 and in situ data. *Remote Sensing of Environment*, *189*, 211–222.
- Ardhuin, F., Rogers, E., Babanin, A., Filipot, J.-F., Magne, R., Roland, A., et al. (2010). Semi-empirical dissipation source functions for wind-wave models: Part I, definition, calibration and validation. *Journal of Physical Oceanography*, *40*(9), 1917–1941.
- Ardhuin, F., Sutherland, P., Doble, M., & Wadhams, P. (2016). Ocean waves across the Arctic: Attenuation due to dissipation dominates over scattering for periods longer than 19 s. *Geophysical Research Letters*, *43*, 5775–5783. <https://doi.org/10.1002/2016GL068204>
- Asplin, M. G., Galley, R., Barber, D. G., & Prinsenber, S. (2012). Fracture of summer perennial sea ice by ocean swell as a result of arctic storms. *Journal of Geophysical Research*, *117*, C06025. <https://doi.org/10.1029/2011JC007221>
- Banner, M. L., Babanin, A. V., & Young, I. R. (2000). Breaking probability for dominant waves on the sea surface. *Journal of Physical Oceanography*, *30*, 3145–3160.
- Bennetts, L. G., Alberello, A., Meylan, M. H., Cavaliere, C., Babanin, A. V., & Toffoli, A. (2015). An idealised experimental model of ocean surface wave transmission by an ice floe. *Ocean Modelling*, *96*, 85–92.
- Bennetts, L. G., & Squire, V. A. (2012). On the calculation of an attenuation coefficient for transects of ice-covered ocean. *Proceedings of the Royal Society of London A*, *468*, 132–162.
- Cole, D. M. (1995). A model for the anelastic straining of saline ice subjected to cyclic loading. *Philosophical Magazine A*, *72*, 231–248.
- Cole, D. M., & Dempsey, J. P. (2004). In situ sea ice experiments in McMurdo Sound: Cyclic loading, fracture, and acoustic emissions. *Journal of Cold Regions Engineering*, *18*(4), 155–174.
- Cole, D. M., & Durrell, G. D. (1995). The cyclic loading of saline ice. *Philosophical Magazine A*, *72*(1), 209–229.
- Cole, D. M., & Durrell, G. D. (2001). A dislocation-based analysis of strain history effects in ice. *Philosophical Magazine*, *81*(7), 1849–1872.
- Cole, D. M., Johnson, R. A., & Durrell, G. D. (1998). Cyclic loading and creep response of aligned first-year sea ice. *Journal of Geophysical Research*, *103*(C10), 21,751–21,758.
- Collins, C. O., Rogers, W. E., & Lund, B. (2017). An investigation into the dispersion of ocean surface waves in sea ice. *Ocean Dynamics*, *67*, 263–280.
- Collins, C. O. III, Rogers, W. E., Marchenko, A., & Babanin, A. V. (2015). In situ measurements of an energetic wave event in the Arctic marginal ice zone. *Geophysical Research Letters*, *42*, 1863–1870. <https://doi.org/10.1002/2015GL063063>
- de Carolis, G., Olla, P., & Pignagnoli, L. (2005). Effective viscosity of grease ice in linearized gravity waves. *Journal of Fluid Mechanics*, *535*, 369–381.
- de Laplace, P. S. (1776). Suite des recherches sur plusieurs points du système du monde (XXV–XXVII) (pp. 542–552). Mém. Présentés Acad R. Sci. Inst. France.
- Dee, D. P., Uppala, S. M., Simmons, A. J., Berrisford, P., Poli, P., Kobayashi, S., et al. (2011). The ERA-Interim reanalysis: Configuration and performance of the data assimilation system. *Quarterly Journal of the Royal Meteorological Society*, *137*, 553–597.
- Doble, M. J., & Bidlot, J.-R. (2013). Wave buoy measurements at the Antarctic sea ice edge compared with an enhanced ECMWF WAM: Progress towards global waves-in-ice modelling. *Ocean Modelling*, *70*, 166–173.
- Dumont, D., Kohout, A., & Bertino, L. (2011). A wave-based model for the marginal ice zone including a floe breaking parameterization. *Journal of Geophysical Research*, *116*, C00E03. <https://doi.org/10.1029/2010JC006682>
- Filipot, J.-F., & Ardhuin, F. (2012). A unified spectral parameterization for wave breaking: From the deep ocean to the surf zone. *Journal of Geophysical Research*, *117*, C00J08. <https://doi.org/10.1029/2011JC007784>
- Fox, C., & Squire, V. A. (1994). On the oblique reflexion and transmission of ocean waves at shore fast sea ice. *Philosophical Transactions of the Royal Society of London A: Mathematical, Physical and Engineering Sciences*, *347*(1682), 185–218.
- Glen, J. W. (1955). The creep of polycrystalline ice. *Proceedings of the Royal Society of London A*, *228*(18), 519–538.
- Grant, W. D., & Madsen, O. S. (1979). Combined wave and current interaction with a rough bottom. *Journal of Geophysical Research*, *84*, 1797–1808.
- Horvat, C., & Tziperman, E. (2015). A prognostic model of the sea-ice floe size and thickness distribution. *The Cryosphere*, *9*, 2119–2134.
- Kohout, A. L. (2008). Water wave scattering by floating elastic plates with application to sea-ice (PhD thesis). University of Aukmant.
- Kohout, A. L., & Meylan, M. H. (2008). An elastic plate model for wave attenuation and ice floe breaking in the marginal ice zone. *Journal of Geophysical Research*, *113*, C09016. <https://doi.org/10.1029/2007JC004434>
- Kohout, A. L., Williams, M. J. M., Dean, S. M., & Meylan, M. H. (2014). Storm-induced sea-ice breakup and the implications for ice extent. *Nature*, *509*, 604–607.
- Li, J., Mondal, S., & Shen, H. H. (2015). Sensitivity analysis of a viscoelastic parameterization for gravity wave dispersion in ice covered seas. *Cold Regions Science and Technology*, *120*, 63–75.
- Liu, A. K., Holt, B., & Vachon, P. W. (1991). Wave propagation in the marginal ice zone' model predictions and comparisons with buoy and synthetic aperture radar data. *Journal of Geophysical Research*, *96*(C3), 4605–4621.
- Liu, A. K., & Mollo-Christensen, E. (1988). Wave propagation in a solid ice pack. *Journal of Physical Oceanography*, *18*, 1702–1712.
- Masson, D., & LeBlond, P. H. (1989). Spectral evolution of wind-generated surface gravity waves in a dispersive ice field. *Journal of Fluid Mechanics*, *202*(7), 43–81.
- Mellor, M. (1986). Mechanical behavior of sea ice. In M. Mellor (Ed.), *The Geophysics of Sea Ice* (pp. 165–281). US: Springer.
- Meylan, M. H. (2002). The wave response of an ice floes of arbitrary geometry. *Journal of Geophysical Research*, *107*(C1), 3005. <https://doi.org/10.1029/2000JC000713>
- Meylan, M. H., Bennetts, L. G., & Kohout, A. L. (2014). In situ measurements and analysis of ocean waves in the antarctic marginal ice zone. *Geophysical Research Letters*, *41*, 5046–5051. <https://doi.org/10.1002/2014GL060809>
- Meylan, M. H., & Masson, D. (2006). A linear Boltzmann equation to model wave scattering in the marginal ice zone. *Ocean Modelling*, *11*, 417–427.
- Montiel, F., Squire, V. A., & Bennetts, L. G. (2016). Attenuation and directional spreading of ocean wave spectra in the marginal ice zone. *Journal of Fluid Mechanics*, *790*, 492–522.
- Mosig, J. E. M., Montiel, F., & Squire, V. A. (2015). Comparison of viscoelastic-type models for ocean wave attenuation in ice-covered seas. *Journal of Geophysical Research: Oceans*, *120*, 6072–6090. <https://doi.org/10.1002/2015JC010881>
- Nghiem, S. V., Rigor, I. G., Clemente-Colón, P., Neumann, G., & Li, P. P. (2016). Geophysical constraints on the antarctic sea ice cover. *Remote sensing of Environment*, *181*, 281–292.
- Nye, J. F. (1953). The flow law of ice from measurements in glacier tunnels, laboratory experiments and the Jungfrau firm borehole experiment. *Proceedings of the Royal Society of London A*, *219*(1139), 477–489.
- Perignon, Y., Ardhuin, F., Cathelain, M., & Robert, M. (2014). Swell dissipation by induced atmospheric shear stress. *Journal of Geophysical Research: Oceans*, *119*, 6622–6630. <https://doi.org/10.1002/2014JC009896>

- Pete, M. A., Meylan, M. H., & Chung, H. (2004). Wave scattering by a circular elastic plate in water of finite depth: A closed form solution. *International Journal of Offshore and Polar Engineering*, 14, 81–85.
- Robin, G. D. Q. (1963). Wave propagation through fields of pack ice. *Philosophical Transactions of the Royal Society A*, 255, 313–339.
- Rogers, W. E., Thomson, J., Shen, H. H., Doble, M. J., Wadhams, P., & Cheng, S. (2016). Dissipation of wind waves by pancake and frazil ice in the autumn Beaufort Sea. *Journal of Geophysical Research: Oceans*, 121, 7991–8007. <https://doi.org/10.1002/2016JC012251>
- Sakov, P., Counillon, F., Bertino, L., Lisæter, K. A., Oke, P. R., & Korabiev, A. (2007). TOPAZ4: An ocean-sea ice data assimilation system for the North Atlantic and Arctic. *Ocean Science*, 8, 633–656.
- Squire, V. (2007). Of ocean waves and sea-ice revisited. *Cold Regions Science and Technology*, 49(2), 110–133.
- Squire, V., Dugan, J., Wadhams, P., Rottier, P., & Liu, A. (1995). Of ocean waves and sea ice. *Annual Review of Fluid Mechanics*, 27(3), 115–168.
- Stopa, J. E., Arduin, F., & Girard-Arduin, F. (2016). Wave climate in the arctic 1992–2014: Seasonality and trends. *The Cryosphere*, 10, 1605–1629.
- Stroeve, J., Holland, M. M., Meier, W., Scambos, T., & Serreze, M. (2007). Arctic sea ice decline: Faster than forecast. *Geophysical Research Letters*, 34, L09501. <https://doi.org/10.1029/2007GL029703>
- Strong, C. (2012). Atmospheric influence on Arctic marginal ice zone position and width in the Atlantic sector, February–April 1979–2010. *Dynamic Coastal*, 39, 3091–3102.
- Sutherland, G., & Rabault, J. (2016). Observations of wave dispersion and attenuation in landfast ice. *Journal of Geophysical Research: Oceans*, 121, 1984–1997.
- The WAVEWATCH III[®] Development Group (2016). User manual and system documentation of WAVEWATCH III[®] version 5.16, *Tech. Note 329*.
- Thomson, J., & Rogers, W. E. (2014). Swell and sea in the emerging Arctic Ocean. *Geophysical Research Letters*, 41, 3136–3140. <https://doi.org/10.1002/2014GL059983>
- Toffoli, A., Bennetts, L. G., Meylan, M. H., Cavaliere, C., Alberello, A., Elsnab, J., & Monty, J. P. (2015). Sea ice floes dissipate the energy of steep ocean waves. *Geophysical Research Letters*, 42, 8547–8554. <https://doi.org/10.1002/2015GL065937>
- Tolman, H. L. (2003). Treatment of unresolved islands and ice in wind wave models. *Ocean Modelling*, 5, 219–231.
- Tolman, H. L., & Booij, N. (1998). Modeling wind waves using wavenumber-direction spectra and a variable wavenumber grid. *Journal of Atmospheric & Oceanic Technology*, 6, 295–309.
- Wadhams, P. (1973). Attenuation of swell by sea ice. *Journal of Geophysical Research*, 78(18), 3552–3563.
- Wadhams, P. (1986). The seasonal ice zone. In N. Untersteiner (Ed.), *The geophysics of sea ice* (pp. 825–991), NATO ASI Series. Boston, MA: Springer.
- Wadhams, P., Hughes, N., & Rodrigues, J. (2011). Arctic sea ice thickness characteristics in winter 2004 and 2007 from submarine sonar transects. *Journal of Geophysical Research*, 116, C00E02. <https://doi.org/10.1029/2011JC006982>
- Wadhams, P., Squire, V. A., Ewing, J. A., & Pascal, R. W. (1986). The effect of the marginal ice zone on the directional wave spectrum of the ocean. *Journal of Physical Oceanography*, 16, 358–376.
- Wadhams, P., Squire, V. A., Goodman, D. J., Cowan, A. M., & Moore, S. C. (1988). The attenuation rates of ocean waves in the marginal ice zone. *Journal of Geophysical Research*, 93(C6), 6799–6818.
- Wang, R., & Shen, H. H. (2011). Gravity waves propagating into an ice-covered ocean: A viscoelastic model. *Journal of Geophysical Research*, 115, C06024. <https://doi.org/10.1029/2009JC005591>
- Williams, T. D., Bennetts, L. G., Squire, V. A., Dumont, D., & Bertino, L. (2013a). Wave-ice interactions in the marginal ice zone. Part 2: Numerical implementation and sensitivity studies along 1D transects of the ocean surface. *Ocean Modelling*, 71, 92–101.
- Williams, T. D., Bennetts, L. G., Squire, V. A., Dumont, D., & Bertino, L. (2013b). Wave-ice interactions in the marginal ice zone. Part 1: Theoretical foundations. *Ocean Modelling*, 70, 81–91.
- Zhang, J., Stern, H., Hwang, B., Schweiger, A., Steele, M., Stark, M., & Graber, H. C. (2016). Modeling the seasonal evolution of the Arctic sea ice floe size distribution. *Elementa: Science of the Anthropocene*, 4, 126.